Use of Depth Imaging for Non-Destructive Testing of Aircraft

a project presented to
The Faculty of the Department of Aerospace Engineering
San José State University

in partial fulfillment of the requirements for the degree
Master of Science in Aerospace Engineering

by

Marina Baltz

December 2021

approved by

Dr. Maria Chierichetti
Faculty Advisor

ABSTRACT

Use of Depth Imaging for Non-Destructive Testing of Aircraft
Marina Baltz

This paper discusses the process in which a damage detecting algorithm was developed and tested. With the use of 3D cameras, a point cloud of a vehicle could be captured. That point cloud could then be visualized and processed using Meshlab, and further analyzed using MATLAB. The algorithm used to detect damage is based off vector analysis and uses a common vector angle formula to determine the angle of each surface normal vector relative to the neighboring vectors. Several images were collected and tested, including real-world examples collected from B737 and A320 aircraft. Simply shaped objects were also tested, although more complex shapes produced better results.

ACKNOWLEDGEMENTS

To my family, thank you for the laughs and for going insane with me. I'm “collage edjumacated” now, ya'll can retire. To my partner, Anu, thank you for all the nights fixing my tattered and broken code. Thank you for allowing me to bounce all my half-brained ideas off you. And thank you for riding this wave with me. To my friends, thank you for letting me ghost you for months at a time without even a drop of judgement. Thank you for the drinks, the food, and the love. To my advisor, Dr. Maria Chierichetti, thank you for being the type of mentor I thought only existed in movies. Thank you for your patience, and your patience, and your patience.

Table of Contents

List of Figures

ABBREVIATIONS

Symbol	Definition
2D	Two-Dimensional
3D	Three-Dimensional
ASIC	Application Specific Integrated Circuit
FAA	Federal Aviation Administration
ICP	Iterative Closest Point
IR	Infrared
LIDAR	Light Detection and Ranging
MSE	Mean Squared Error
MX	Maintenance
NDT	Non-Destructive Testing
NRMSE	Normalized Root Mean Squared Error
RGB	Red, Green, and Blue
RMSE	Root Mean Squared Error
SDK	Software Development Kit
SLAM	Simultaneous Localization and Mapping
UAM	Urban Air Mobility
UAV	Unmanned Aerial Vehicle

1. Introduction

Aircraft encounter stress causing events every day, and these events bring opportunities for the formation of damage. The very purpose for which an aircraft is created, flying, causes constant stress on the body of the structure, with additional stress and strain occurring during takeoff and landing. Environmental factors can range from extreme temperature changes to lightning and bird strikes. Aircraft servicing procedures require industrial equipment to be driven directly up to the fuselage. Multiple pieces of equipment are also attached directly to the aircraft. To ensure the airworthiness of the aircraft and the safety of all those onboard, exterior surface inspections are conducted frequent.

A walk around the perimeter of the aircraft allows ground crew, pilots, and maintenance personnel to verify that the aircraft is safe to fly and that there are no unaccounted defects on the exterior surface of the fuselage. This basic type of aircraft exterior inspection was developed in the 1930s [1] and has not been significantly updated since its creation [2]. Inspection methods have grown with advancing technology, yet the aviation industry has fallen behind in the utilization of these methods. The goal of this project is to use the advancements in inspection methodology and demonstrate their effectiveness in aircraft exterior inspections.

1.1 Approaches for Non-Destructive Testing

Inspections can be conducted for reasons beyond determining if there are imperfections in a structure. They can be used to collect a variety of information on a material, from age, density, weight, strength, and so on. There are three general method categories for material inspection. The three methods are divided by their degree of invasiveness [3]:

- Destructive
- Semi-Destructive
- Non-Destructive

Destructive inspection approaches are where the material being tested is significantly damaged to the point where it is no longer usable [3]. To determine the age of a tree, the tree can be cut down and the growth rings on the stump can be counted. This process is a form of destructive testing as the tree will no longer grow after it has been cut down and the test can only be conducted once [4] [5].

Semi-destructive methods are where damage is contained to a portion of the material, or the damage is superficial [3]. Again, taking the example of the age of a tree, rather than cutting down the tree to count the growth rings, a sample of the core can be taken with the use of a boring tool. The core sample provides the same information without significantly damaging the tree. The tree can continue growing and additional tests can be conducted.

The non-destructive method ensures no damage occurs to the tested material and can be conducted as many times as necessary so that results can be verified and validated [3]. To

determine the age of a tree without damaging it in any form, a tape measure can be used to measure the circumference of the tree. The diameter of the tree can be determined from the circumference. The diameter can then be multiplied by the growth factor of the species of tree to give an approximate age [5, 6]. This inspection method is an approximation, but it is an accepted method for tree dating.

Non-destructive methods can be contact or non-contact in their application. Contact means that to test or inspect the material, equipment needs to physically touch the material. Non-contact means that the material can be inspected without physically touching anything. Contact inspections often require equipment and controlled environments, making them impractical for use during flight operations. Contact methods are more effectively conducted during extensive maintenance inspections. Non-contact methods can provide more flexibility depending on the specific test conducted and equipment required. For this reason, non-contact equipment less inspections are commonly used for inspections required during flight servicing operations.

There are many non-destructive tests in use today; most tests fall within the following techniques [7, 8, 9]:

- Ultrasonic
- Magnetic Particle
- Radiological
- Electromagnetic
- Acoustic Emission
- Liquid Penetrant
- Leak Testing
- Visual

Each method and the most common use cases will be briefly described. Depending on the relevance of the research, some test methods may be covered more in depth than others.

1.1.1 Ultrasonic Testing

Ultrasonic testing is conducted with the use of high frequency sound waves and is applied either via pulse-echo or through-transmission [10, 11]. The pulse-echo method involves the use of a transducer that outputs and receives the high frequency sound wave energy. When using this method during aircraft maintenance inspections, line plots are produced to display the signal depth through the tested material [12]. The signal depth data can also be interpreted by a computer to produce a two-dimensional image, called a sonogram [13].

The through-transmission method uses an emitter to output ultrasound waves from one side of the material to a receiver on the other side. Defects are detected because they cause a reduction in the amount of sound received [14]. Ultrasonic tests provide immediate results and can be portable or automated. The sound waves used in ultrasonic testing are highly sensitive to extremely small defects and are highly penetrating, allowing for the detection of defects deep in the component [15, 16]. However, this method does not perform well on materials that are thin, rough, or irregularly shaped. This inspection method also requires that the surface be cleaned and

any loose materials, such as chipping paint, be removed. Ultrasonic testing is performed on materials such as ceramics, plastics, metals, concrete, and composites. This method is not recommended for use on wood or paper materials [17]. Ultrasonic testing on aircraft is considered a non-destructive contact maintenance inspection.

1.1.2 Magnetic Particle Testing

Magnetic particle testing allows users to detect imperfections through the examination of disruptions in the magnetic field within a material [7]. Ferromagnetic materials such as iron, nickel, and steel, are highly susceptible to magnetization [18]. To perform the magnetic particle test, these materials are induced with a magnetic field. Disruptions to the magnetic field flow are made visible by covering the surface of the material in iron particles. Disruptions in the flow cause the iron particles to collect in certain areas [10]. The size and shape of the defect can be outlined directly on the part. This is an indication of imperfections in the material [18].

Magnetic particle testing is a fast and effective inspection method for detection of surface and subsurface defects. This method has been found to be a highly reliable method of testing for high stress aircraft components, such as parts that rapidly rotate or vibrate [18]. Surface defects on irregularly shaped components can also be detected with this method.

One limitation of this method is that it does not work on materials that are non-ferromagnetic such as gold, silver, and copper. Because these materials are not magnetic, the iron particles will not adhere to them, and imperfections in the material will not be detected [7]. There are also positional limitations as magnetic fields are directional and must be perpendicular to the defect for best results. Magnetic particle testing on aircraft is considered a non-destructive contact maintenance inspection [7, 18].

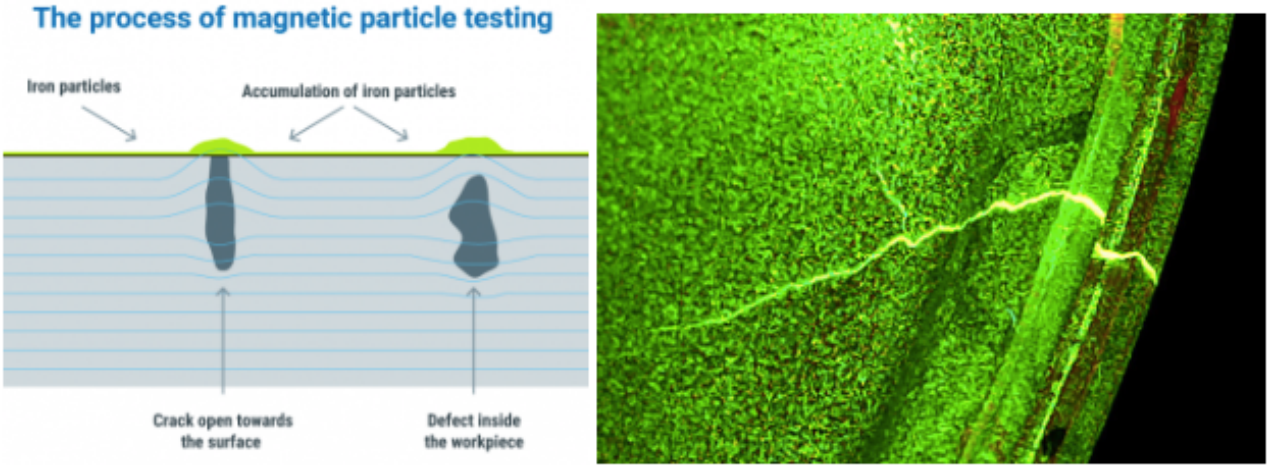

Figure 1.1: (Left) Magnetic particle testing diagram *[19]* (Right) Crack detected using fluorescent magnetic particle testing *[20]*

1.1.3 Radiological Testing

Radiological methods of inspection use gamma or X-radiation to identify material defects. Radiation is directed from either a radioactive isotope or an X-ray generator, to the test material. The radiation penetrates through the material and onto a film or another type of detector, creating a shadowgraph [7]. A shadowgraph displays underlying aspects of the test material. Shadowgraphs are commonly referred to as x-rays, and are often used in a diagnosis involving bones or joints [21].

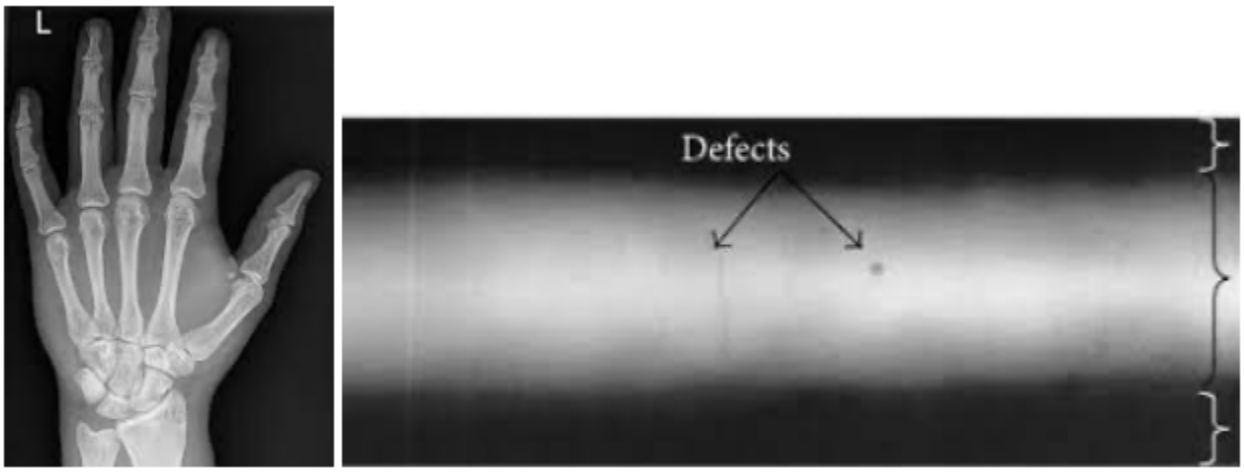

Figure 1.2: (Left) Hand X-ray *[21]* (Right) Shadowgraph of welded seam with defects *[22]*

Radiological inspections can be conducted on virtually any material if access to both sides of the object is available. The inspections do not require any form of disassembly and create permanent records of results. This inspection can be used to determine a variety of internal characteristics such as cracks, corrosion, loose fittings, and debris, however this method has minimal sensitivity to fine cracks and defects [8]. Using radiation is a hazardous process and any unnecessary personnel must be cleared from the room in which the inspection is conducted [7, 10]. Between equipment set up and protecting personnel, set up time can become lengthy. Radiological testing on aircraft is considered a non-destructive contact maintenance inspection [18].

1.1.4 Electromagnetic Testing

An electromagnetic inspection test is conducted by measuring the strength of electrical currents in the magnetic field around a conductive test material. Interruptions in the magnetic field allow inspectors to make judgements about the material and possible defect locations [23]. Eddy-current testing, a specific type of electromagnetic test, is commonly used to detect corrosion and cracks near the surface of aircraft fuselages [24]. An eddy-current test is performed by exciting a conductive wire coil with alternating current. This causes the coil to create a magnetic field that oscillates at the same frequency as the alternating current. Currents that are opposite to those in the coil, called eddy currents, are induced when the coil is placed near the conductive test material [10].

Electromagnetic testing is a quick, portable, and highly sensitive inspection method that requires minimal part preparation [25]. It can be used to detect surface and subsurface

imperfections however it can only be applied to conductive materials, such as aluminum, or iron. Non-conductive materials like rubber, plastic, or paper cannot be tested with electromagnetic inspection methods [8]. Electromagnetic testing on aircraft is considered a non-destructive contact maintenance inspection.

1.1.5 Acoustic Emission Testing

Acoustic emission testing is essentially the opposite of ultrasonic testing. Rather than creating and sending sound waves through a material, acoustic testing listens for materials creating and emitting sound energy. The bursts of acoustic emissions are produced by defects in the test material. The location, intensity, and duration of the sound can reveal additional information about the defect as well. During flights, aircraft components that are under active stress are often fitted with transducers to detect acoustic emissions signifying the formation of a defect [26, 27].

Defects and failures can be detected and recorded during periods of unattended monitoring with acoustic emission testing [17]. Types of detectable acoustic emissions include impacts, fiber breakages, friction, and more. Additionally, these emissions can be detected under hazardous operational conditions such as high temperatures, high pressures, corrosive environments, and nuclear environments [28]. Acoustic emission testing is used to determine the structural integrity or general health of a component, however further testing is usually required to fully diagnose an issue. This method relies on the emission of stress energy from a defect, this leads to imperfections that are not actively moving or growing to not be detected [10]. Acoustic emission testing on aircraft is considered a non-destructive contact inspection that can be conducted during either maintenance or flight operations.

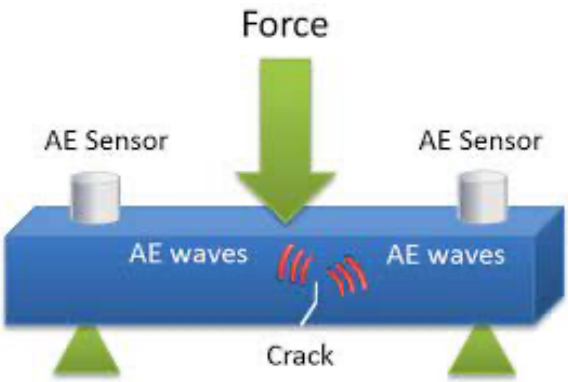

Figure 1.3: Diagram of acoustic emission method *[29]*

1.1.6 Liquid Penetrant Testing

Liquid penetrant testing is the process by which a material is coated in a liquid dye solution to detect defects in the material. The solution flows into any cracks or other types of defects that may be along the surface [7]. Any excess coating solution is removed from the material so only the liquid that has penetrated the defects along the surface is visible.

For high sensitivity evaluation of a component, fluorescent penetrants can be used to detect very small discontinuities along the surface [30]. Liquid penetrant testing is an inexpensive, quick, and portable inspection method that is commonly used to confirm the presence of defects. It can be used directly on the surface of an aircraft or on individual components, however cleaning the test area before and after inspection is required [10]. The penetrant test works best on materials that have a smooth surface and can only be performed on materials that are non-porous [8]. The liquid penetrant method can have difficulties when applied to areas that have been welded as the welds make it difficult to remove excess solution and can result in false indications of imperfections. Liquid penetrant testing on aircraft is considered a non-destructive contact maintenance inspection [18].

For high sensitivity evaluation of a component, fluorescent penetrants can be used to detect very small discontinuities along the surface [30]. Liquid penetrant testing is an inexpensive, quick, and portable inspection method that is commonly used to confirm the presence of defects. It can be used directly on the surface of an aircraft or on individual components, however cleaning the test area before and after inspection is required [10]. The penetrant test works best on materials that have a smooth surface and can only be performed on materials that are non-porous [8]. The liquid penetrant method can have difficulties when applied to areas that have been welded as the welds make it difficult to remove excess solution and can result in false indications of imperfections. Liquid penetrant testing on aircraft is considered a non-destructive contact maintenance inspection [18].

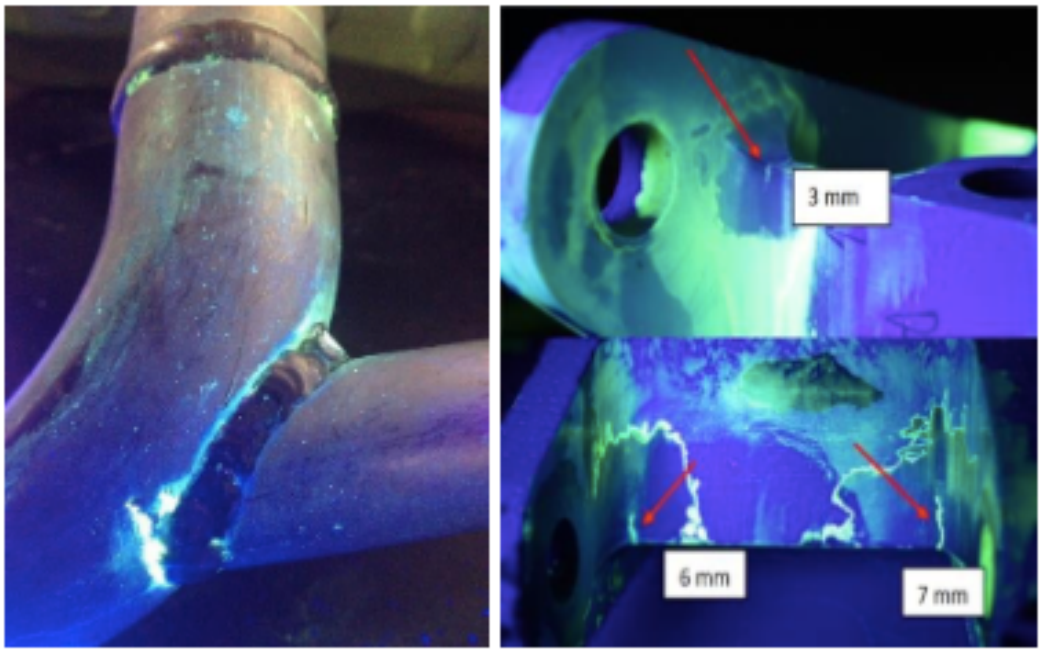

Figure 1.4: (Left) Welded exhaust pipe *[31]* (Right) Cracked landing gear fork *[32]*

1.1.7 Leak Testing

The leak testing method works on pressurized or vacuum systems to identify the location of a physical hole in the material, also known as a leak. Leak testing equipment can range from

high tech listening devices to simple soap and water mixtures that produce bubbles when coated over a leak. Leak tests are commonly performed on pressurized and vacuum systems [10].

The advantages and limitations vary greatly depending on the type of leak test conducted. For instance, when testing a pressurized gas component, the part is submerged in an inexpensive fluid, such as water, and does not require clean up after. However, when testing a pressurized liquid, either expensive equipment is required or the leaks are visible and require clean up [33]. Leak testing on aircraft would be categorized as a non-destructive contact maintenance inspection.

1.1.8 Visual Testing

Visual inspection methods are the number one most commonly used non-destructive testing method [7, 34]. This method of inspection is also one of the most basic forms of inspection as it often does not require any tools to perform. Visual testing is performed with the human eye, however tools such as flashlights or cameras can also be used when a view is obstructed. According to the Federal Aviation Administration (FAA), visual inspections account for more than 80 percent of the inspections conducted on large transport category aircraft. The FAA also states that the smaller the aircraft, the more the visual inspection method is used [34].

A visual inspection is the process of using the human eye, with or without the use of various aids, as the primary sensing device from which judgments can be made about the state of an inspected material. Visual inspections are used to assess the overall condition of a component, structure, or system [10]. They are also useful for early damage detection, as they are performed at frequent intervals and allow defects to be discovered before critical size is reached [8]. The visual inspection method is also used to obtain additional information when signs of a defect are discovered within a component or process. Subsurface flaws are not detectable via visual inspection methods alone and small flaws can be difficult to detect.

Table 1.1: Summary of NDT methods

Method	Contact	Operation Type	Damage Size	Location	Advantages	Limitations
Ultrasonic	Yes	MX	Extremely small	Subsurface	Immediate results, equipment is portable, process can be automated	Material must conduct sound well
Magnetic Particle	Yes	MX	0.5 micrometer for wet systems	Near or on surface	Fast, effective, and highly reliable	Ferro-magnetic materials only

			and 5micrometers for dry systems			
Radiological	Yes	MX	Minimal sensitivity to fine cracks and defects	Subsurface	Able to detect flaws as small as 2% of the thickness	Non-porous materials only
Electromagnetic	Yes	MX	Highly sensitive to small cracks	Near or on surface	Quick, portable, and highly sensitive	Metal materials only
Acoustic Emission	Yes	MX or Flight	Defects must be actively growing or moving	Surface or subsurface	Can analyze entire structure	Equipment is expensive, results can be difficult to interpret
Liquid Penetrant	Yes	MX	Smallest detectable damage size is 3mm	Surface	Inexpensive, quick, and portable	Non-porous materials only
Leak Testing	Yes	MX	Any size as long as the damage fully penetrates through the material	Surface	Can analyze pressurized or vacuum systems	Expensive equipment or clean up required
Visual	No	MX or Flight	Can vary depending on the equipment used	Surface	Inexpensive, and quick	Smaller flaws can be difficult to detect

1.2 Image Based Inspections: A Visual Method

In regards to commercial aircraft, safety is often touted as the number one priority of airlines [35], however to stay in business airlines do need to turn a profit. Aircraft that are not flying, are not generating revenue [36]. Therefore, when it comes to aircraft inspections, speed and reliability are necessary. From the different types of non-destructive testing methods reviewed, visual inspections are the most heavily relied upon method due to the speed and ease of the inspection process [34]. Visual techniques, specifically image-based inspection methods, will therefore be the focus of this project.

Image based inspection is the process by which objects are scanned with a camera to detect anything from catastrophic failures to minor quality defects. These inspections can be performed manually or autonomously and can be used in conjunction with a variety of camera types depending on the material being inspected and the type of defect being detected [37]. Depending on the use case, the camera can provide live feed to the inspectors or collect still images for analysis. The use of image-based detection in conjunction with artificial intelligence has grown immensely popular over the last few years as vehicle manufacturers have been incorporating the technology into their vehicles as part of the autopilot system [38].

Image based inspection systems are also increasingly being used in concrete crack detection. With the use of visualization software in conjunction with digital images, researchers have developed a method to inspect concrete bridges for cracks [39, 40, 41]. The method involves collecting two-dimensional (2D) images and using an image stitching algorithm to "stitch" the 2D images together to create a three-dimensional (3D) model of the object scanned. The 2D images can be pre-processed to enhance the image quality of the 3D model through spatial or frequency domain operation. Once the images have been stitched together, an algorithm can be used to identify cracks. The authors determined that using a generic crack property extraction algorithm on the images was not a feasible solution, so instead they used an edge detection algorithm. Initial testing of crack width led to less than desirable results with the error ranging from 0.21 - 48.17\%. It was then determined that using a supervised neural network model would produce better results. With the use of 101 crack patterns, a neural network, a computing system that consists of artificial neurons, was trained to recognize, and detect cracks. The neural network results produced significantly better results with an improved error range of 4.12 - 15.54\%. This process of using large amounts of images to train artificial neural networks to recognize objects or patterns is commonly referred to as machine learning [40].

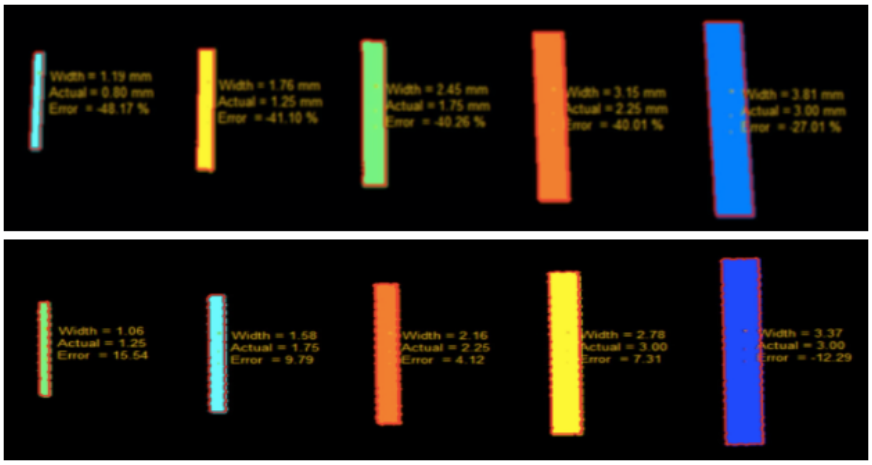

Figure 1.5: (Top) Results from edge detection method. (Bottom) Results from neural network method *[40]*

Although machine learning can be extremely useful, it requires massive amounts of example data to train the neural network [42, 43]. This is often a slow, tedious, and heavy workload. To overcome these problems, researchers have proposed to apply change detection approaches for structural inspection. The method of change detection begins with establishing a baseline representation of the structure undergoing inspection [40]. The baseline can then be used for future inspections to be compared against. Any damage to the structure will present itself as a change when compared to the baseline [44]. Adopting change detection methods can help reduce the data processing workload when used prior to damage detection approaches, as textures and joints that may otherwise appear as a false positive, can be addressed in the change detection stage. Change detection techniques can be divided into two main categories, point cloud and image-based change detection methods [40, 44].

A point cloud is a collection of coordinate points within a space. The point cloud-based change detection method defines the baseline structure as a point cloud. When produced properly, point clouds can be very accurate. Subsequent inspection scans are aligned and compared with the baseline point cloud. The alignment typically occurs with the use of the iterative closest point (ICP) algorithm. The ICP algorithm is integrated into several open-source point cloud processing software. It is worth noting that the change in depth must be significant enough to be identified in the first place. If the damage is too shallow or simply does not create sufficient geometric change, the alternative image-based change detection methods can be implemented [44].

Image based change detection is like point cloud-based change detection approaches, except rather than comparing point clouds, images are compared. Before this method is applied, image pre-processing is required to remove environmental variations. Once pre-processing and change detection methods are completed, damage detection techniques can then be developed [40, 44].

1.3 Camera Types

The method described above is an example of the use of a regular camera. A standard digital camera will output a 2D image made up of pixels. Each pixel is given a Red, Green, and Blue (RGB) value. Each pixel displays a color based on those RGB values and together the pixels form the image captured by the camera [45].

Another type of camera that has potential for use in structural inspections is the stereo camera. A stereo camera operates similarly to a regular camera; however, a stereo camera has two or more lenses to capture images with simultaneously. By having more than one lens the camera can simulate human vision and capture 3D images. When an image is captured with a stereo camera, the image again contains RGB data, but it also contains depth data. The depth data is given in the form of coordinate [45, 46].

An additional image capturing device is the depth camera. The depth camera employs the use of a stereo camera along with some additional components. A depth camera often has four different components. The first component is an RGB module that can sense and collect color information. The second is an infrared (IR) projector. The IR projector works by creating a pattern of infrared dots that are projected onto an object [45]. The human eye is unable to perceive the infrared dots, but the camera can, as it is equipped with two IR cameras. Because there are two IR cameras, the two components can also be referred to as a singular IR stereo camera. The infrared dots help to produce a point cloud, a collection of data points within a space. With a depth camera, each point in the point cloud has an RGB value as well as an additional depth value. The depth value is the distance measured from the object being captured to the depth camera [47].

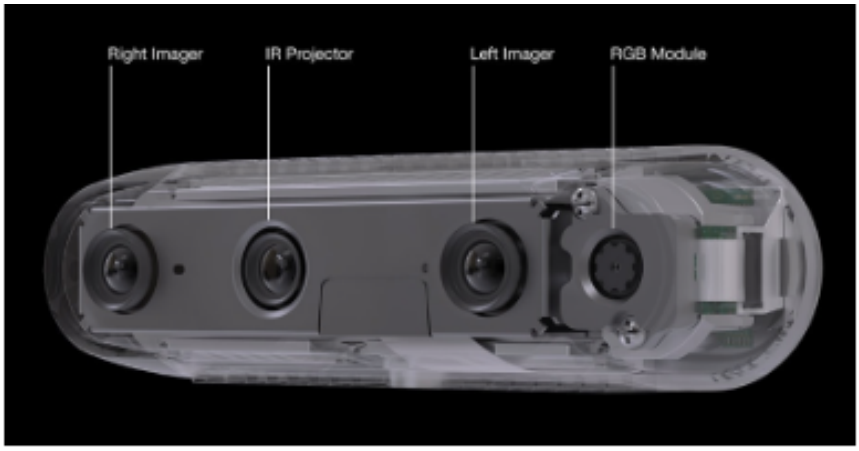

Figure 1.6: Intel RealSense D435 depth camera *[48]*

1.4 UAV Camera Based Inspection Approaches

All the visual inspection methods and camera types discussed thus far can be implemented upon an unmanned aerial vehicle (UAV) such as a quadcopter or drone. Researchers have begun to use such tools and methods to inspect infrastructure [49, 50, 51, 52].

Some have even gone so far as to incorporate autonomous flight into the UAV vision-based inspection system [41].

To use a UAV in conjunction with a camera requires the inspector to account for the movement of the UAV during the scanning process. To obtain the drone's absolute position, GPS data is commonly utilized as it provides the required information for autonomous flight. However, interference is a common problem with GPS usage, as radio signals from satellites are not well received when the drone is near infrastructure such as buildings. This creates a feasibility issue considering that the drones were specifically designed to inspect social infrastructure and are required to autonomously fly near buildings safely. To counteract this issue, researchers developed an algorithm and integrated it into the inspection system to estimate the position of the drone [41].

To develop the location estimation algorithm, a 3D depth camera was utilized to extract depth and image data of the surrounding environment. A simultaneous localization and mapping (SLAM) algorithm used the depth information to estimate the position of the drone. The researchers also developed a controller to autonomously control the drone based on the produced position information [41].

In the case of the research, there were no 3D maps provided for autonomous navigation. This meant that the UAV was required to create the map of its environment while simultaneously estimating its position within that same environment. The specific camera used was a depth camera developed by Intel, the ZR300. This camera could update its position 30 times per second using the sensor data received from the depth camera. Although 3D maps were not provided initially, it was proposed that the UAV could conduct two flights for inspection purposes. A preliminary flight that would be used to capture environmental data and to construct a map for autonomous navigation. The second flight would use the constructed map to conduct the structural inspection along a predetermined path [41].

1.5 Relevance

Current exterior inspections for general and commercial aircraft are conducted via a walkaround. Pilots and ground crew walk around the perimeter of the aircraft to visually inspect the exterior for damage. This process is highly reliant on the human eye and the surfaces of the vehicle that are not visible from the ground, are completely neglected. Additionally, these inspections are almost always conducted outside, where weather conditions often lead to visual impairments. Exterior structural inspection methods have not kept up with modern technology.

Several studies have been conducted on the use of UAVs for structural monitoring. However, there is a clear lack of UAVs being used to inspect aluminum or composite structures such as an aircraft. The studies that do exist, focus on steel and concrete structures such as bridges [40, 43, 49, 50, 51]. One study that specifically used UAV monitoring for aircraft panels, used a combination of penetrant coating and powder developer, contact-based inspections, to be able to highlight a damaged area with an ultraviolet light. The process described in the study is highly accurate but intensive and slow. The use of computer vision-based sensing technology in conjunction with machine learning practices are rapidly evolving [53]. However, these methods still require the collection and creation of large data sets as example material, a tedious and

laborious task. To create crack detection and localization algorithms has been studied in civil engineering and is a more appropriate method for aircraft structural monitoring.

By developing an aircraft exterior structural monitoring system, an opportunity is created for the entire process to become automated and the human factor to be removed significantly. Ground crew and pilots will no longer need to carry the responsibility of ensuring an aircraft has been thoroughly inspected. A baseline for damage detection can be achieved and standardized for use across multiple vehicle models and manufacturers.

1.6 General Methodology

With the use of computer vision software such as MATLAB, three-dimensional images can be displayed and analyzed. The human eye is able to look at these images and determine if there is an abnormality such as a variation in the shape of the object that is not within the normal bounds of the object [54]. The proposal for this project is to use computer vision applications to display 3D images and develop analysis software to detect abnormalities. MATLAB will be the primary computer vision application used to achieve this goal.

Currently, there is not a readily available function or algorithm for reliable damage detection. To develop one, there are three options worth mentioning but only one that will be explored in detail. Machine learning technology is rapidly developing and could be used to teach a program to recognize damage. This method requires a massive amount of sample images to use as part of the learning process [42]. For this reason alone, machine learning will not be explored.

By collecting images of an undamaged object and the same object with damage, the images can be compared and any similarities can be subtracted, this process is called image subtraction [55]. If successful, this method would produce an image of the damaged area. This requires two images that are very similar which may lead to issues with different camera angles or other environmental changes. Additionally, images must be taken of the object before damage has occurred. This may not always be possible for aircraft.

A change detection method would detect any significant changes in the depth of an object [44]. This method may be simple in theory but may not work as well with complex objects such as aircraft. The change detection method will be the primary method focused on regarding the purposes of this project as well as image subtraction as an alternative.

Once the equipment needed to collect depth images is acquired, the algorithm development can begin. Both an Intel RealSense D435 depth camera and Apple's TrueDepth camera are available and capable of capturing depth images within a usable scope. From there, MATLAB will be utilized to detect significant changes in the shape of the object. There are several MATLAB functions that can aid in the visualization and analysis of depth images.

2 How Everything Works

2.1 Depth

This project will involve the use of an IR stereo camera and Apple's iPhone 12. The cameras are used to measure the distance of an object from the camera and to create a 3D image of the object. To better understand how the cameras function, each system will be broken down and discussed in detail.

2.1.1 IR Projector

To create a depth map, infrared light as part of a pattern projector is commonly used. Infrared light is not visible to the human eye and is not susceptible to environmental lighting requirements. An IR camera can capture IR light in well-lit and dark environments [56].

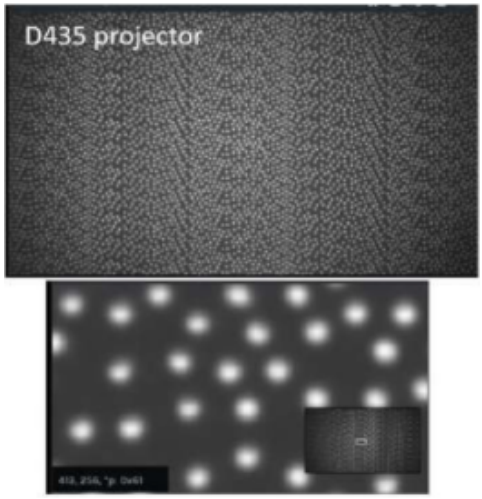

Figure 2.1: Intel RealSense D435 depth camera IR dot pattern [57]

The D435 depth camera uses an IR stereo camera as well as a pattern projector to generate a depth map. As is common with stereo cameras, the D435 operates by capturing images simultaneously from the left and right cameras, measuring the disparity between matched pixels, and generating a depth map from the disparity and pinhole model triangulation. The D435 is considered an active stereo vision system. This means that the system relies on an optical projector to overlay the environment with a semi-random texture that aids in the pixel correspondence process. The D435 uses an AMS Princeton Optronics projector that has a wider emission angle and fewer dots projected than other D400 series cameras. The depth algorithm that the D435 uses is capable of picking up the slightest textures in an environment [57].

For D400 series cameras, Intel places the IR pattern projectors in between the left and right cameras. The patterns do not need to be strictly stable and when additional IR patterns are projected onto the same object the overall performance of the D435 improves as additional light and texture are projected onto the object [57]. This was an important factor when comparing depth cameras, as similar low-cost depth cameras rely on structured or coded light and have strong requirements regarding the stability of the projected pattern over time.

Range and precision are the key depth camera performance parameters for the purposes of this project. The camera will need to be, at an absolute minimum, a drone propeller's length away from the object if implementation is ever expected to reach synergetic capabilities with a drone. The range of a depth camera is determined by the fill ratio, the percentage of pixels that have a non-zero depth value. The further the camera from the object, the lower the fill ratio, and therefore the less effective the system is at measuring depth. By relying solely on the IR pattern projector embedded in the D435 camera, fill ratio becomes a limitation in the maximum operating range. To maintain a minimal payload weight for potential drone integration, the use of additional IR pattern projectors will not be considered within the scope of this project [57].

Each pixel in an image contains data such as color, brightness, or depth, depending on the type of image captured. Image noise is the random variation of that data and is usually caused by a sensor or the circuitry of the camera. Noise in depth images is often defined as the Root Mean Squared Error (RMSE or RMS error) of a plane fit measured flat wall. This depth noise is normalized into a value that is independent of the camera's range. The normalized value is referred to as the subpixel resolution, or precision.

RMSE is the square root of the Mean Squared Error (MSE) and measures the change per pixel caused by equipment processing and is calculated using equation 2.1 below [58].

$$RMSE = \sqrt{\frac{1}{M*N}\sum_{i=0,j=0}^{M-1,N-1}[I(i,j) - K(i,j)]^2} \qquad (2.1)$$

M is the image width, N is the image height, K(i, j) is the original image, I(i, j) is the enhanced image, and i and j are the pixel coordinates. To normalize the RMSE it is common to divide it by the range of the measured data as shown in equation 2.2 [59].

$$NRMSE = \frac{RMSE}{y_{max} - y_{min}} \qquad (2.2)$$

A lower normalized RMSE (NRMSE) value indicates fewer residual variances. These variances can appear as bumps on the image and lead to less precise measurements. Figure 2.2 below compares a point cloud measured on a flat surface taken at two different NRMSE values.

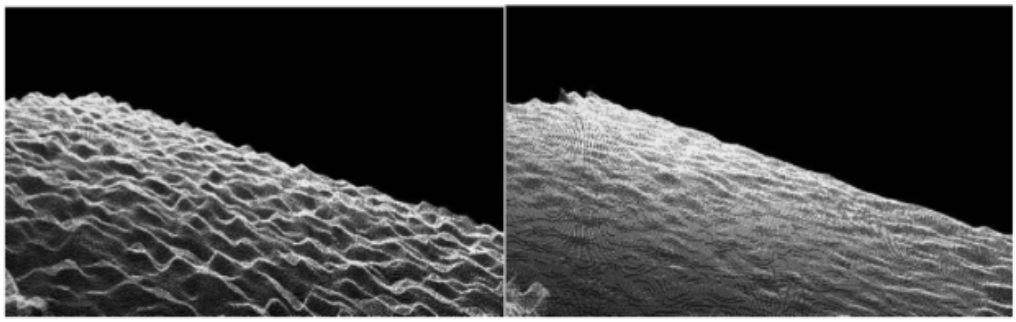

Figure 2.2: (Left) Depth noise from point cloud measured from a flat wall. (Right) Depth noise from the same surface, captured at a 3x lower NRMSE value.

The application-specific integrated circuit (ASIC) that the Intel D400 series cameras use has a minimum quantization step of 0.032 pixels. IR pattern projectors onboard the D435 camera produce a subpixel RMS error between 0.07 - 0.11. When measuring the depth units, the ASIC defaults to a 16-bit depth and sets the depth unit to 1 mm. This gives the camera a maximum range of 65 m. For the scope of this project, a range of 65 m is excessive considering that it is larger than the wingspan of a Boeing 747 aircraft [60]. The range will be adjusted by changing the “depth units" setting in the Intel RealSense SDK 2.0 (software development kit) that comes with the D435 camera. For example, the depth units can be changed from the default 1 mm setting to 0.1 mm, thus changing the range from 65 m to 6.5 m [57].

2.1.2 Stereo Camera

Stereo cameras function similarly to human eyes. Humans have binocular vision which allows depth to be perceived using two eyes. Stereo cameras can simulate binocular vision using two or more lenses. Each lens also has an individual image sensor. The Intel D435 depth camera that is used for this project has two lenses.

Stereo camera lenses often have a distance of 6.50 cm between them [61]. This is the average distance between human eyes, known as the intra-ocular distance. The distance between two camera lenses is referred to as the intra-axial distance. The greater the intra-axial distance, the more dramatic the three-dimensionality effect becomes.

A person can be standing directly in front of a cube yet only see a two-dimensional square. If the person takes a step to one side of the object, the point of view changes, and a three-dimensional cube becomes visible. Every step around the object that is taken, alters what is seen by the person. Stereo vision was developed around this phenomenon, in which multiple projections of a 3D object appear depending on one’s view of the object [62]. By capturing images of the same object from two or more different points of view, the object can be reconstructed in a 3D space.

Stereo cameras can take a pixel from one image and find the corresponding pixel in another image. This matching of pixels helps to create a disparity map, a map of the differences in pixel location [63]. These disparity maps are what allow the 3D object to be reconstructed and is where many of the stereo computation problems lie. Stereo cameras are able to create 3D objects not only through the use of two or more lenses but through their corresponding point searching algorithms [62].

Stereo matching algorithms are either global or local. Global algorithms involve resource exhausting computations and are performed offline. Local algorithms can provide real-time 3D reconstructions but are less accurate [64]. The D435 camera uses local algorithms to provide real-time results. The exact algorithms used by the D435 and other RealSense cameras are the intellectual property of Intel, and are therefore not accessible to the public. It is not possible to discuss the specific algorithms used in the D435 depth camera.

A discussion regarding the general process used in stereo cameras is still necessary for a complete understanding of how depth is calculated. Stereo vision systems answer two general questions. The first being, which pixel in the left image corresponds to which pixel in the right image. This is referred to as pixel correspondence. The second question it answers is, what is the real-world location of the corresponding points. This is referred to as object reconstruction [65, 66]. The more robust the pixel correspondence, the better the quality of the 3D reconstruction [64].

Stereo reconstruction methods use the pinhole camera model, in conjunction with parallel geometry. A pinhole camera in its most basic form is a light-proof box with a pin sized hole on one side. Light from the point of focus passes through the pinhole and projects the display onto the opposite side of the box. The pinhole model is the relationship between the object's coordinates in a 3D space and the display projected onto the image plane of an ideal pinhole camera.

Given two coordinate points through pixel correspondence algorithms, the depth can be estimated using the disparity between the two points. With the two sets of coordinate points, the 3D space coordinates, X, Y, and Z, can be computed as shown in equation 2.3.

$$X = \frac{x_L * b}{d}, Y = \frac{y_L * b}{d}, Z = \frac{f * b}{d} \quad (2.3)$$

Where x_L and y_L refer to the set of coordinate points extracted from the left image, and x_R, and y_R refer to the set from the right image. The variable *b* refers to the intra-axial distance measured in millimeters, *d* is the disparity $d = x_L - x_R$ measure in pixels, and *f* is the camera lenses focal length measured in pixels [62, 67].

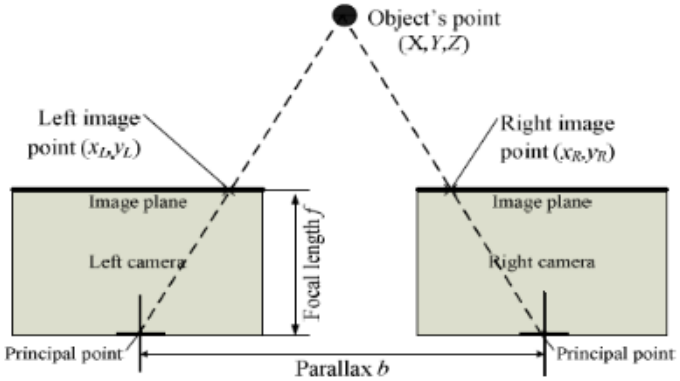

Figure 2.3: Stereo geometry illustration *[62]*

2.1.3 Apple's TrueDepth Technology

The Intel D435 calculates depth by projecting an IR pattern onto an object and capturing a left and right image of the object, measuring the pattern distortion and pixel disparity, and using that information to calculate the depth of the object from the camera. Apple's iPhone X and later use similar technology and equipment with some important differences. An iPhone 12 Pro will be used to capture depth images and will from here on be referred to simply as an iPhone.

Rather than having two IR cameras to capture an IR pattern projected over an object, the iPhone has one IR camera and one standard camera. In addition to an IR pattern projector, the iPhone has a flood illuminator, and an ambient light sensor. The iPhone is also equipped with a light detection and ranging (LIDAR) camera that will not be utilized for this project as it determines depth via time-of-flight measurements making it far less accurate [68].

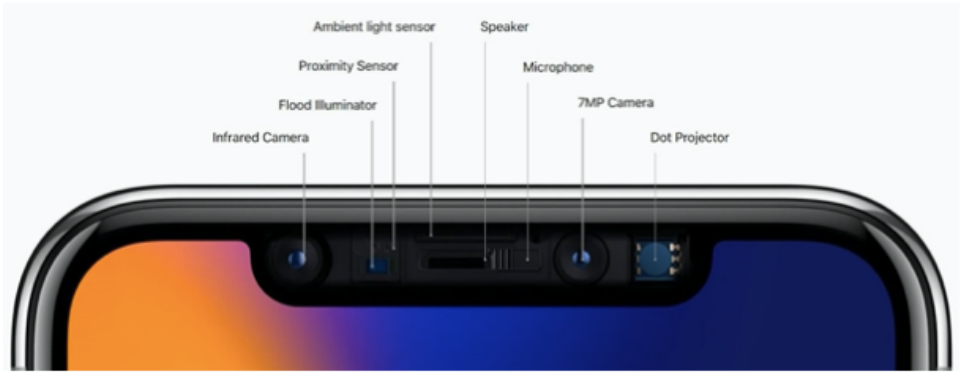

Figure 2.4: Breakdown of front facing components on Apple's iPhone 12 Pro *[69]*

Similarly, to the D435, Apple's TrueDepth technology is privately-owned intellectual property and therefore certain information such as point matching algorithms and even system accuracy is unknown. The TrueDepth system is an integral part of iPhone's Face ID verification security system and is only capable of creating 3D maps of user faces. To use the iPhone for 3D scanning of objects, a third-party application is required [70].

iPhone's TrueDepth system works similarly to the Intel D435 camera. The flood illuminator uses IR light to confirm the presence of a face or object. The pattern projector then projects a device specific pattern of 30,000 IR dots over the object. The IR camera then captures multiple 2D images of the IR pattern over the object and sends the image data to the application processor. The processor generates a mathematical model and a 3D map is created which can be exported into processing programs such as MeshLab or MATLAB [71].

2.2 Visual Functions

MATLAB is a commercially available software used for high-level technical computing developed by MathWorks. MATLAB is a programming language environment that provides visualization, computation, and interfacing tools to users. It is considered more advantageous for technical problem solutions than conventional programming languages [72].

MATLAB is advantageous as it does not require dimensioning of arrays and has powerful functions readily available for use within the MATLAB workspace. Graphic commands are simple to use and provide immediate visualization results. There are also add-on toolboxes that contain functions and interfaces for a variety of industry specific applications. MathWorks provides free documentation on most of the MATLAB functions, explaining how the code works and providing some common use cases. Additionally, it is common for universities to have license agreements with MATLAB that allow students to use limited versions of the program for classroom purposes [72].

2.2.1 MATLAB Functions

Many of the MATLAB functions that will be used within the scope of this project will provide visualization and calculation information. Each function used as part of this project will be discussed briefly. Functions that are used solely for formatting purposes will not be mentioned here.

Functions such as stem3 and quiver3 are used to plot 3D coordinates, however the way the two functions operate varies even though the plots may appear similar. The stem3 function plots discrete sequence data by extending the z-coordinate data from the xy coordinate plane [73]. The quiver3 function outputs a vector plot with arrows. The arrows display the directional components defined by the 3D coordinates. By default, this function scales the length of the arrows so that they do not overlap [74].

Surf and surfnorm are 3D surface plot functions. To produce a 3D surface, the z-coordinate points are taken as the height and plotted above the plane defined by the x- and y-coordinates. In a surf plot the z-coordinates are also used to determine the color of the surface, changing as the z values do [75]. In addition to this, a surfnorm plot calculates the surface normals and displays them with red lines protruding from the surface. Imaginary lines that are perpendicular to the tangent plane at a point of a non-flat surface are referred to as surface normals [76].

There are also functions that can be used to determine the position or the change in position between points. The isInside function is used to determine if a specified point is within a selected set of boundaries [77]. The isChange function can be used to find significant changes in the data. To be considered an abrupt change, a vector of data must be split into two segments. The original vector can be referred to as A, and the segments can be referred to as A1 and A2. In equation 2.4 below, τ is the threshold parameter given by the user, and C is the cost function. A cost function is the measure of how well a segment is approximated by its mean value. If the sum of the iterated cost functions is larger than the cost function of the vector, then MATLAB considers the change in points to be abrupt [78].

$$C(A1) + C(A2) + \tau < C(A) \tag{2.4}$$

2.2.2 Image Subtraction/Point Cloud Comparison

Another depth detection method that is worth mentioning is image subtraction. Image subtraction involves the input of two images to output a third image. In image subtraction, the output image is the first image minus all the corresponding pixels from the second image. Basic image subtraction uses 2D images and depending on the desired results can output an image containing just the differences, the reference image minus all the differences, or the reference image minus a constant value [79]. In relation to this project, image subtraction can be used to detect a change in depth as it brings attention to areas that are not common between the two images. This method is susceptible to the detection of other variances such as pixel color or environment changes. However dissimilarities can also be the result of a change in depth [79].

Point clouds are 3D models; therefore, the 2D image subtraction method becomes a point cloud comparison method. The point cloud comparison method requires two-point clouds or two triangular mesh models. The two models must be the same scale and have the same origin point. Once the models are appropriately lined up the distances between the two models can be measured. Certain open-source programs such as CloudCompare are capable of comparing a point cloud to a mesh, as well as a point cloud to a point cloud and a mesh to a mesh [80]. Used by itself, this method would likely require human verification of individual results. For this reason, the image subtraction method will not be considered as a primary means of damage detection.

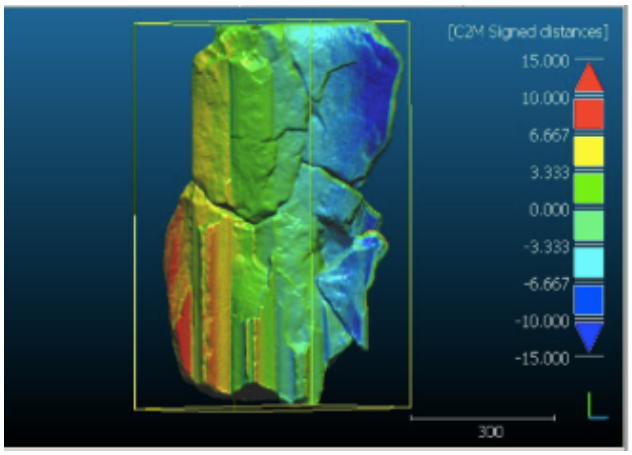

Figure 2.5: 3D entity comparison results with color scale. *[80]*

2.3 Calibration and Setup

The D435 depth camera comes factory calibrated. Self-calibration is possible but Intel recommends against it unless the camera has experienced a fall or some sort of damage [81]. There are no known calibration methods for the iPhone, however the iPhone does not need to be calibrated as is usable out of the box. For the scope of this project, the D435 and iPhone 12 Pro factory calibration will be used.

Although calibration was not necessary for either camera, there were some setup options that required changing. To capture normal 2D RGB images with the iPhone, the camera image capturing format was changed from the "High Efficiency" setting to "Most Compatible." The "High Efficiency" setting is primarily used to reduce file size and conserve storage space. The setting was changed to output a JPEG file rather than an HEIC file which is not compatible with many computer programs, including LaTeX editors.

For 3D depth capturing with the iPhone, an app called Heges was used. Heges can capture images with the iPhone's front facing IR camera, or the back facing LIDAR camera. The app can export 3D image files as a GLB, STL, or PLY file.

A Binary Graphics Language Transmission Format or GLB is a 3D file format used primarily in Virtual and Artificial Reality. It is also commonly used for game and web app development. GLB files are small, load quickly, and can support texture, shadow, and animation data [82, 83].

Standard Triangle Language or STL was created to be used with CAD software [84, 85]. It is primarily used for 3D printing, prototyping, and manufacturing [86]. The STL format does not store color or texture data and is only capable of describing the surface geometry of a 3D object. STL files use 3D Cartesian coordinate unit normals and vertices to describe an unstructured triangulated surface. However, the units are arbitrary, and no scaling information is contained within an STL file [87].

Polygon file format or PLY was designed specifically to store 3D data collected via 3D scanners. The descriptive data of a single object is stored as a list of nominally flat polygons. Information regarding the color, transparency, surface normals, and texture coordinates are stored with the PLY format [88]. It is the only Heges file format that will store RGB color data. The PLY file format will be used to export images from Heges as PLY will store the necessary data and is compatible with software such as MeshLab and MATLAB.

3 Reference Object Image Collection

3.1 Reference Material

To ensure both cameras are working properly a few reference images are collected. By collecting images of undamaged objects with the D435 and iPhone, a baseline can be developed for reference and comparison. Capturing images of the same object with both cameras will also provide a direct comparison of each camera's capabilities.

3.1.1 Material Comparison

The fuselage of a commercial aircraft is commonly made up of aluminum and aluminum alloys. The exterior layer of an aircraft is often referred to as the 'skin' of an aircraft as it expands and contracts during flight. The skin of an aircraft undergoes stress from cabin pressurization, and shear loads [89]. It is a thin and fragile layer that experiences contact with industrial equipment multiple times a day.

Aluminum square alloy tubing was chosen as an initial reference object because it is a simply shaped object, and the material composition is like that of a commercial aircraft. There are no complex curves, every side is the same length and width, and the surface is smooth. Measuring and marking the object is easily performed with a tape measure and marker which will become useful when creating artificial damage.

Figure 3.1: Manufacturer markings on square aluminum alloy tube.

The square tube material is aluminum alloy 6061-T6. T6 is the temper of the material. Temper is the result of heat treatment and artificial aging of the metal to achieve specific material properties. Regardless of the temper, alloy 6061 has a modulus of elasticity of 69 GPa, or 10,000 ksi [90]. Alloy 6061-T6 has been tempered to achieve its maximum yield strength.

6061-T6 has a maximum tensile strength of 290 MPa, and a yield strength of 240 MPa. The fatigue limit is defined at 97 MPa and 500 million cyclic loads [91].

Alloy 6061-T6 is a primary material used in the skin of light aircraft. The alloy has excellent corrosion resistance properties and is also utilized for miscellaneous low-stress fittings. Alloy 6061-T6 is a preferred material for fuel and oil tanks, pipes, instrument tubes, brackets, and other components that may require welding. Alloy 6061 is also used in hydraulic accessories and heat exchangers [91].

Table 3.1 Alloy 6061 composition [Percent Mass] *[92]*

Al	Mg	Si	Fe	Cu	Cr	Zn	Ti	Mn
95.85-98.56	0.8-1.2	0.4-0.8	0.0-0.7	0.150.4	0.04-0.35	0.00.25	0.00.25	0.00.15

Commercial aircraft use a range of aluminum alloys depending on the location-based requirement of the aircraft. For instance, areas of the aircraft where strength is critical, alloy 7075 is used. For areas that are damage-critical, alloy 2024 is used [93]. Aircraft manufacturers most commonly use aluminum alloy 7050 and 7075 [94, 95].

Aluminum alloy 7050 is used as a commercial aerospace alloy [96]. It is a strong material and is highly resistant to stress cracking. 7050 has a tensile strength of 515 MPa, a Young's Modulus of about 75 GPa, and a fatigue strength of 240 MPa [97]. Alloy 7050 is used in the manufacturing of aircraft wings, fuselages, bulkheads, and other aircraft structures. It is not recommended for welded areas as the welding process can weaken the alloy [98].

Table 3.2 Alloy 7050 composition [Percent Mass] *[97, 35]*

Al	Cu	Mg	Zn	Zr
89	2.3	2.3	6.2	0.12

7075 alloy has excellent strength, ductility, and toughness, and has a good fatigue resistance. It also has a significantly higher corrosion resistance than 2000 series alloys. Alloy 7075 is more likely than other aluminum alloys to become brittle as a result of micro segregation [99]. 7075 is one of the most used materials in aircraft structural manufacturing and is especially used for high stress components. Alloy 7075 has a tensile strength of 572 MPa, a Young's Modulus of 72 GPa, and a fatigue strength of 159 MPa [100].

Table 3.3 Alloy 7075 composition [Percent Mass] *[100]*

Al	Zn	Mg	Cu	Fe	Si	Mn	Cr	Ti
87.1 - 91.4	5.1 - 6.1	2.1 - 2.9	1.2 - 2	0.0 - 0.5	0.0 - 0.4	0.0 - 0.3	0.18 - 0.28	0.0 - 0.2

3.2 Undamaged Aluminum

The reference object is an 11-inch piece of square aluminum alloy tubing with a cross-section of 2 in by 2 in. The aluminum alloy skin of commercial aircraft averages a thickness between 1 mm to 2.2 mm [93]. The square aluminum tubing has a similar thickness of 0.125 in.

Four reference objects will be used for this project, three of which will be purposefully damaged as part of the depth image collection experiment process. The fourth square tube will be used as a control piece.

Although the difference in material properties between the 7000 series alloys and the 6061 alloy is significant, alloy 6061 is still usable as a reference material. The material properties are not as important as the way the depth cameras view the material. The surface and reflectiveness of the material are more significant factors when it comes to image quality and depth accuracy.

Figure 3.2 below shows the different views available given the iPhone and D435 depth capturing devices. The top image is a mesh model rendered from the point cloud captured with the iPhone via the Heges application. Comparing the 3D model to the standard 2D RGB image in the bottom left, there is some noise in the 3D model. Additionally, the word "Reference" appears to be out of focus which may be an indication of noise or poor image quality. Capturing images with the Heges app was difficult at times and many unusable models were produced before a quality model was captured.

The bottom right image in Fig. 3.2 shows the color scaled 2D depth map of the undamaged reference object. The image was captured using the D435 depth camera. Similarly, to the image captured with Heges, there is noise in the areas that appear to be reflective. When looking at the 2D RGB image, the alloy tube is reflecting light on its left end. When looking at the depth map, that same area appears to have no depth data. In the depth map image, the structure to the right of the square tube is a nightstand not captured by the D435 RGB camera.

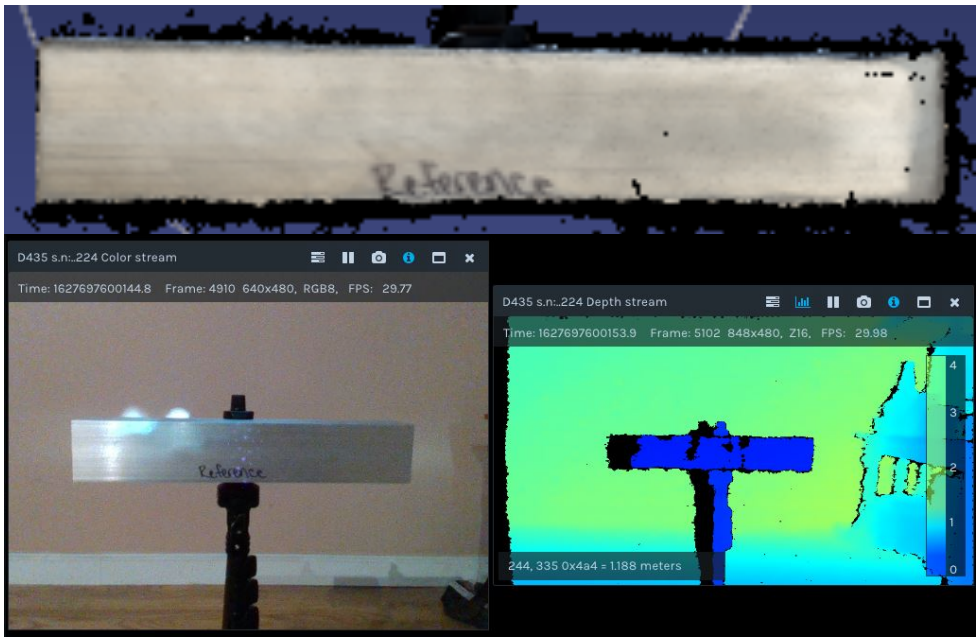

Figure 3.2 (Top) Object captured with iPhone displayed in MeshLab (Bottom) Object captured with D435 displayed in RealSense Viewer

3.3 Creation of Damaged Aluminum

Prior to creating damage on the test objects, reference markings were drawn on the object surface. Lines were drawn 1-inch apart and an additional diagonal line was drawn through 2-inch

sections to create a center point to aim the damage. Below are images of the reference objects before damage along with the items used to create damage.

Figure 3.3: (Top) Hammers. (Bottom) Drill bits

To create damage, the first object was hit with a club hammer, a ball peen hammer, and a claw hammer. The aluminum alloy was surprisingly damage resistant and contact was made multiple times with each hammer. The club and claw hammers were not able to make more than a scuff mark, however the ball peen hammer made a noticeable dent.

For the second object, different sized holes were drilled into the object. The drill bits used were 5/64, 1/8, 5/32, 3/16, and 1/4 inch. A center punch, a tool used to produce a small dimple, was used to minimize the drill bit wobbling and creating a taper rather than a hole. Some minor tapering occurred on the 1/8-inch hole, but the remaining holes were created cleanly. The results of the damage can be seen below.

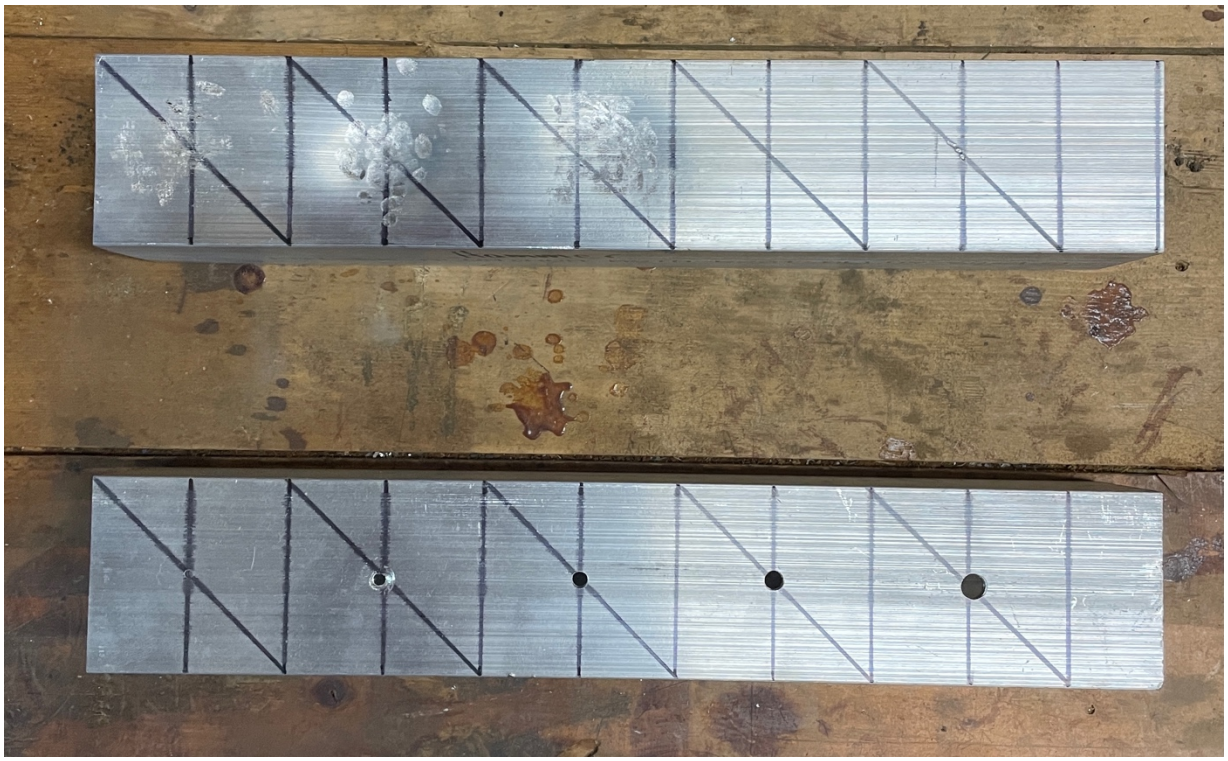

Figure 3.4: (Top) Object with damage from different hammers. (Bottom) Object with various size drill holes

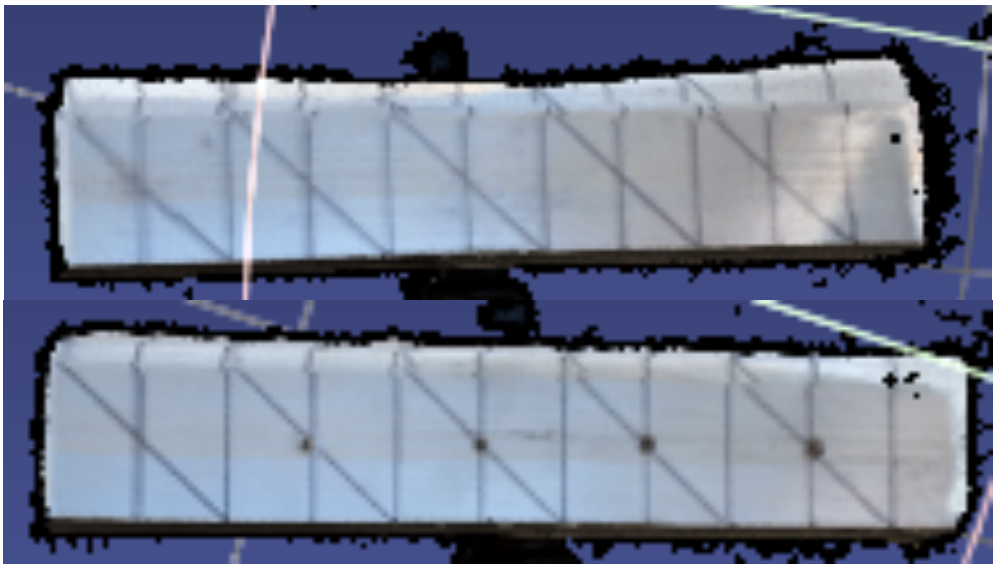

Figure 3.5: MeshLab view (Top) Object with damage from different hammers (Bottom) Object with various size drill holes

Like the images of the undamaged object captured with the iPhone, the damaged objects also appear to have some image quality issues. The reference lines are clearly misaligned at the top of the image. This is likely due to moving the camera either too quickly or at a distance

outside the camera's range. The images were captured outdoors with an even and natural light exposure, and the images do not appear to have reflective areas. Therefore, it is unlikely that lighting caused these issues, as it did in the undamaged images captured by the D435.

Figure 3.6 below shows the two damaged objects captured with the D435 and displayed using Intel's RealSense Viewer. The damage caused by the hammer is visible in the 2D RGB image, however there is no significant indication of this damage in the depth map image. This also appears to be the case for the damage caused by the drill. It is interesting to note that the infrared dot pattern is visible in both RGB images. Although the depth map and mesh models both appear to show no signs of damage, the PLY models will provide better detail once imported into MATLAB.

Considering that multiple scanning attempts were made with two different imaging devices, image quality may become an issue. Neither device produced a clean and crisp image. Images produced with both the iPhone and D435 were noisy, and images produced with the iPhone were misaligned. Most concerning is the 1/4-inch hole that appears to have gone undetected. Poor image quality may make it difficult to accurately measure object depth. Inaccurate depth measurement would therefore result in damage going undetected.

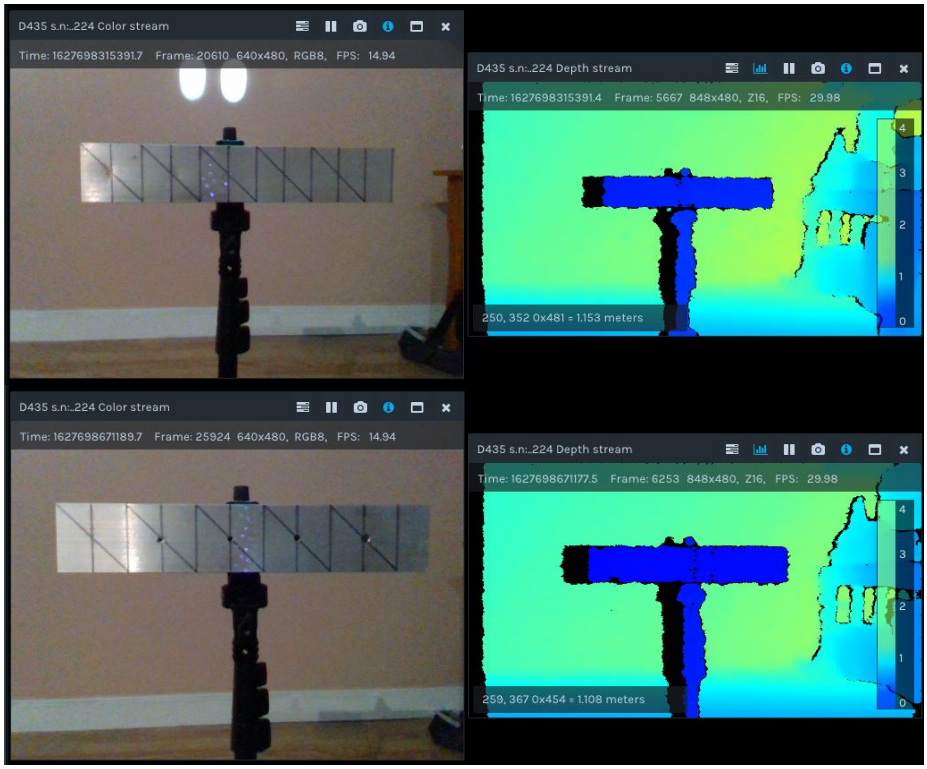

Figure 3.6: Images captured with D435 and displayed using Intel RealSense Viewer (Top) Object damaged with hammers (Bottom) Object damaged with drill holes

3.4 Image Processing

To better allow for the application of software, the images were processed prior to any analyses. To process the images, MeshLab was used. The PLY image files were imported as meshes. From there, several of the "cleaning and repairing" filters were applied. Duplicate faces

and vertices were removed. For reference, from the drilled image, there were no duplicate faces, but there were 1,554,299 duplicate vertices.

Again, using the drilled object as a reference, 3,011 isolated components with diameters smaller than 0.0958 world units were removed. MeshLab works under the assumption that the meshes are unitless, hence the use of world units. By removing isolated components with respect to their diameter, unintentionally captured fragments not part of the focus object, are removed and only the larger, intentionally captured object remains. The 134,642 now unreferenced vertices are also removed. It is important to note that the order in which these filters are applied matters, as removing isolated components prior to removing duplicate vertices can result in the entire mesh being filtered out.

To further aid in the post processing analysis, the lower part of the mesh was removed. The tripod used to hold the square tubing in place is not part of the area being analyzed and was therefore removed. MeshLab allows the user to manually select a section of vertices and delete them, along with the corresponding faces. Although this process seems manual, it will likely not be required in real world applications as an aircraft can hold itself up with the use of landing gear or similar components.

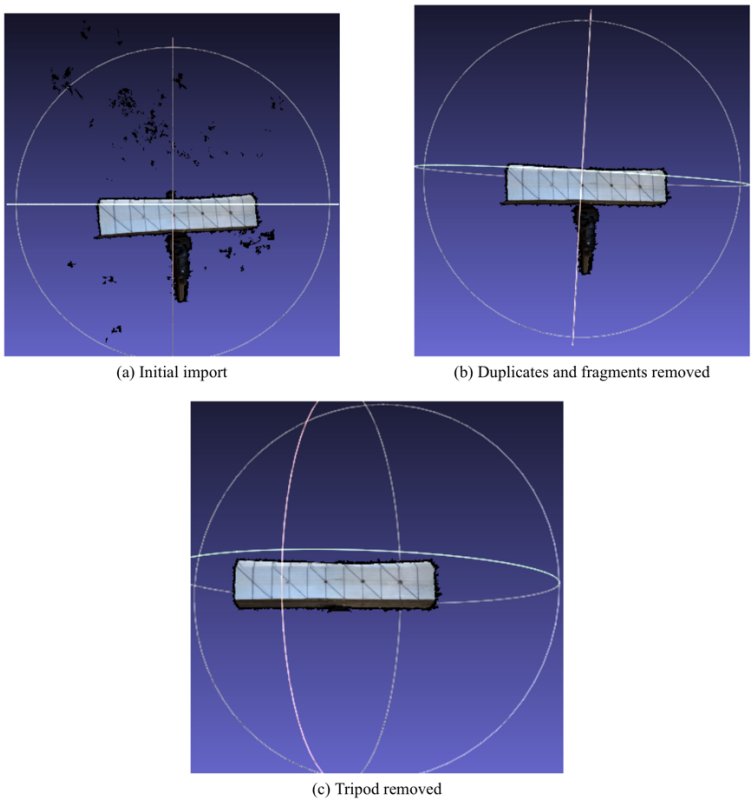

(a) Initial import

(b) Duplicates and fragments removed

(c) Tripod removed

Figure 3.7: Example of image processing steps

4. Collection of Real-World Examples

The purpose of this project is to develop a non-destructive structural inspection method to be used during daily flight servicing operations. To develop a method without testing on an actual aircraft would be insufficient. Images of the undamaged surface from a B737 and A320 are collected to use as reference as well. The images collected are from the lower part of the fuselage and are of a curved, smooth surface. Simply shaped objects and surfaces are preferred to avoid unnecessary complexity.

All images and data collected from aircraft were obtained using only the iPhone 12 Pro, as the D435 requires a physical connection to a computer to operate. This requirement severely limited mobility and was not practical while collecting images in an actively operating airport environment.

Figure 4.1: American Airlines A320

4.1 Undamaged Aircraft References

4.1.1 Component or Damage?

Figure 4.2 below shows three images of an undamaged section of a Boeing 737 aircraft. The yellow lines seen in Fig. 4.2a, have aircraft types, spray painted on the ground next to them, and are used to determine where to park an aircraft based on its type. The images were captured outdoors, at night, with the only source of light coming from the jet bridge, this can be seen in Fig. 4.2a. Considering the conditions in which the images were captured, both images are of fair quality. In the standard RGB camera image, Fig. 4.2b, the fuselage riveting is well defined, the "POTABLE WATER" text is clear and legible, and the drain port has a significant change in depth compared to the curvature of the fuselage. The painted parking spots can even be seen as a reflection in the surface. Figure 4.2c shows the image imported into MeshLab. The drain port will likely result in a false positive.

(a) Ground view

(b) Close-up view

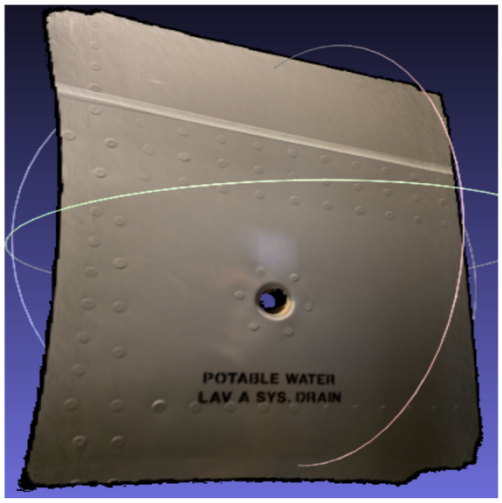

(c) Imported image

Figure 4.2: Undamaged section of B737 aircraft

4.1.2 Undamaged Aircraft Panel

Figure 4.3 below shows an undamaged panel captured from an A319 aircraft. Poor image quality has caused the image to appear textured and rough, especially around the edges. This image has not undergone pre-analysis processing; however, image quality continues to be a challenge of this research. Additionally, smoothing is not recommended as a processing step as damage may be lost.

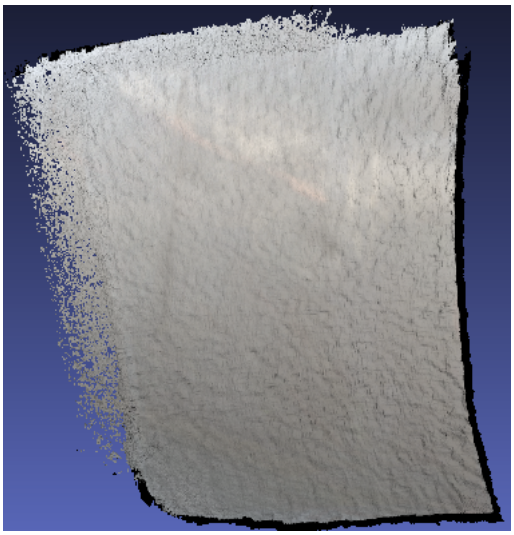

Figure 4.3: MeshLab view of undamaged A319 panel

Fortunately for passengers, there was no damage that resulted in a hole on any of the accessible aircraft. Unfortunately, that means that no images of holes created by damage were captured for analysis. Images of aircraft holes were captured but they are considered as undamaged components.

4.2 Damaged Aircraft Panel

Aircraft damage can occur in a variety of ways. A bird can strike the horizontal stabilizer, or an employee driving a belt loader can hit the aircraft. The latter was likely the cause of the damage shown in Fig. 4.4. The area immediately surrounding a cargo bin is one of the most damaged areas on an aircraft. The damage is approximately 19 mm wide, and 1.5 mm deep. The silver circle directly to the bottom left indicates that this damage was seen and logged by an aircraft mechanic. The damage was determined to be within the acceptable range and the aircraft was deemed to still be airworthy [101].

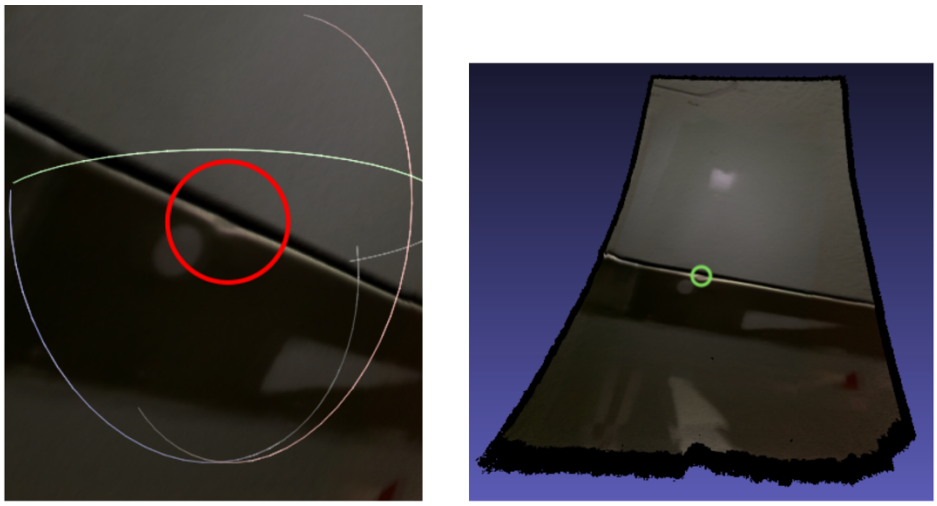

(a) Cargo bin with damage circled in red (b) Full view

Figure 4.4: Damaged B737 cargo bin door

4.3 Thoughts and Decisions

Images captured with the iPhone 12 Pro did not seem to have the same issues as images captured with the D435. Reflectiveness of the object did not inhibit the quality of the image, and the size of the object was not altered by its relation to the background. Camera movement did still have a significant part in the quality of the image. If the iPhone or the D435 are moved too quickly or are brought too closely to the object, the image begins to duplicate over itself and create erroneous overlaps.

Due to the issues encountered while using the D435 camera, moving forward only the iPhone will be used for capturing images. The D435 must be attached to a computer to operate and is limited to the length of the USB cable it is attached to. This restrained movement limits the portability of the D435, as well as the environments in which it can be used.

5. Post-Processing Analysis

At this point, the images have been captured, processed, and are ready to be analyzed. To analyze the images that have been processed in MeshLab, a MATLAB script was written.

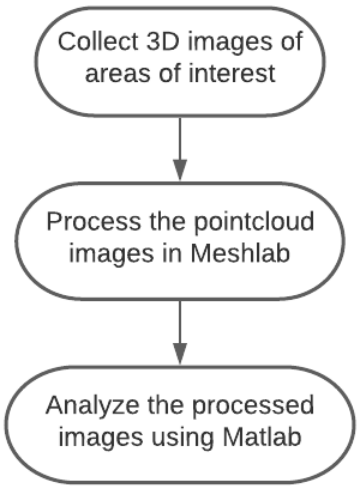

Figure 5.1: Flowchart of major steps in dent detection process

The general theory behind this code is that the surface normals run parallel or nearly parallel to each other. Therefore, if there is a dent or a hole in the surface of an object, those surface normals will no longer be at or near parallel to their neighboring normals. This theory was first developed after using MATLAB's surfnorm and quiver3 functions. The surfnorm function calculates the surface normals. The quiver3 function creates a plot for visualization and displays the direction of the surface normals. This can be seen in Fig. 5.2 below.

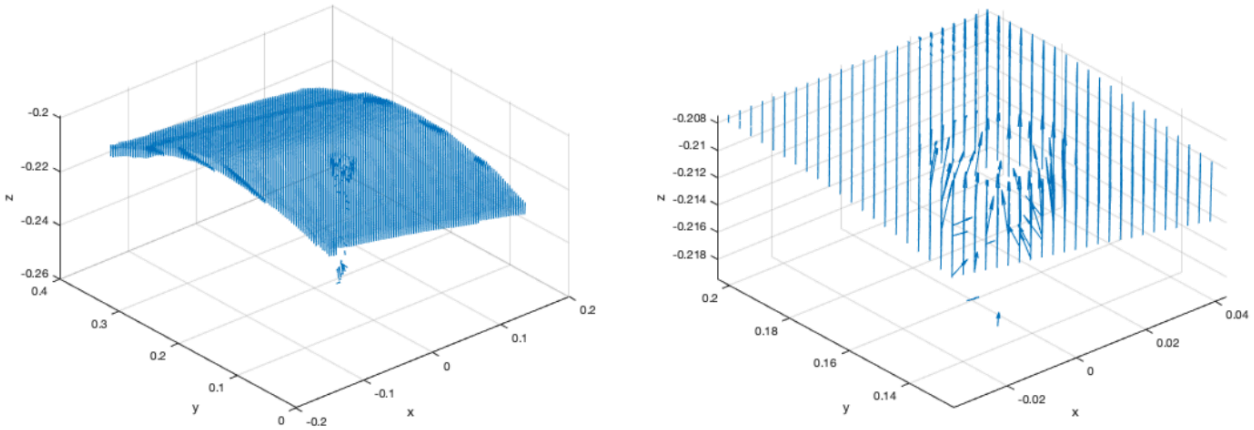

(a) Quiver3 display of surface normals (b) Zoomed in view

Figure 5.2: Quiver3 plots of surfnorm calculated values

5.1 Initial Setup

Images captured with the iPhone result in the creation of PLY file. For those who have MATLAB's Computer Vision Toolbox, there are point cloud specific functions that allow the data to be imported as part of the MATLAB script. Unfortunately, this toolbox was not available during the image analysis process. PLY image data was imported into MeshLab as part of the pre-analysis process, but it was also a necessary step to convert the file type. MeshLab allows users to export the 3D model as a data set of 3D coordinate values.

The data needs to be formatted to meet the requirements of the MATLAB functions. The data is imported as an Nx3 matrix with each column referring to an axis. The data is separated by these axes and a linear step size is defined using the linspace function. From there, MATLAB's meshgrid and griddata functions are used to return grid coordinates. Once the data is properly formatted, two zero matrices are added to store calculated data.

5.2 Using Vector Angles to Detect Damage

With the data formatted and the initial setup of the script completed, the vector analysis can begin. As mentioned previously, the theory motivating this research is that a significant change in vector angles can be used to detect change. To calculate the angle between two vectors, equation 5.1 below was used, where $\vec{u}$ and $\vec{v}$ are vectors, and θ is the angle between $\vec{u}$ and $\vec{v}$. This equation is ideally used when only working with two vectors. However, when working with several thousand vectors, a for loop is necessary. By creating a for loop that cycles through every position in the vector matrices, the difference between each vector pair can be calculated. The matrix that was once filled with zeros can now be filled with the angle values.

$$cos\,\theta = \frac{\vec{u} \bullet \vec{v}}{\|\vec{u}\|\|\vec{v}\|} \qquad (5.1)$$

Lastly, before a cycle is completed and the for loop continues to the next vector pair, a threshold check is needed. At this point, it should be noted that the term threshold here, means a value that must be exceeded to trigger a detection of damage. The threshold values themselves will be in units of degrees as they will be compared to differences in vector angles. By adding a conditional if statement to the loop, a threshold can be manually set. This ensures that each value stored in the angle matrix is compared against the threshold. If the angle is greater than the threshold, a value of one is added to the second zero matrix. Creating a logical matrix of zeros and ones is useful when plotting the areas with detected damage. Once the angle between a vector pair has been calculated, and that angle has been compared against the threshold, then the loop can continue to the next cycle.

5.3 Visualizing the Results

Assuming the number of steps is 100, the process described in the section above results in a 100x100 matrix of zeros and ones. To plot the results, the MATLAB surf function is used to display a surface plot of the XYZ grid coordinates. Another for loop and if statement are used in conjunction with each other to loop through each position in the logical matrix and check if there is a value of one stored. If there is a value of one, the position is used to plot the corresponding XYZ normal position as a scatter plot point. The 3D scatter plot is then displayed

on top of the surface plot. Essentially the surface plot is displaying the object, while the scatter plot highlights that potentially damaged areas. The result will look like Fig. 5.3 below. Additionally, the MATLAB script can be reviewed in appendix A.

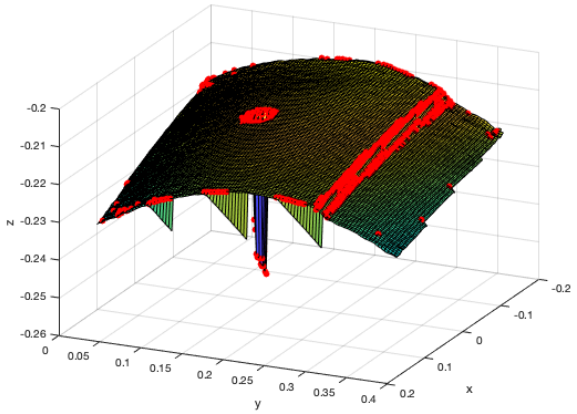

Figure 5.3: Surface plot with red dots highlighting detected areas

6. Description of Results

Results were produced for all the objects examined, from the simply shaped aluminum square tubing to the commercial aircraft. The analysis has proven successful with a surprisingly accurate level of damage detection. The results of the analytical process are discussed in detail below.

6.1 Analysis of the Reference Objects

Before reviewing the damaged reference objects, it is important to first discuss the undamaged reference object to act as a baseline to compare the damaged results against. In Fig. 6.1 below, the edge is clearly detected by the MATLAB script. In Fig. 6.1a, the lower threshold value has caused some additional detection at the top and bottom of the image. The detection at the top appears random and is likely due to surface texture caused by less than perfect image quality. With a higher threshold value, as seen in Fig. 6.1b, the random pattern is no longer detected.

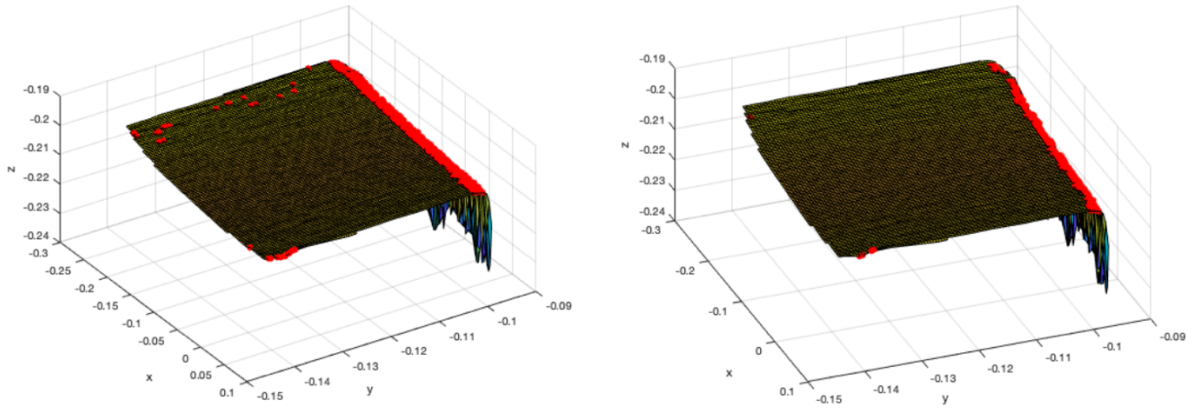

(a) Reference object with a threshold of 5 (b) Reference object with a threshold of 12

Figure 6.1 Reference object result

6.1.1 Analysis of Hammered Objects

In section III, to ensure that testing could be conducted on damaged objects, two lengths of square aluminum tubing were damaged. One object was beaten repeatedly with three different types of hammers and the tip of a screwdriver, and the other object had holes drilled through it. Images of the objects were captured with the iPhone, processed in MeshLab, and analyzed using MATLAB script. The results are discussed below.

Figure 6.2 below shows the results of the hammered object. As seen in Fig. 6.2b, the edges of the square tubing are detected as damage. This is due to the large change in vector angles at the corners, causing a false positive detection of damage. This false positive around the edges of an object occurs for every object and is an expected result, as determined by the

baseline provided by the undamaged reference object. The damaged areas have been circled in green.

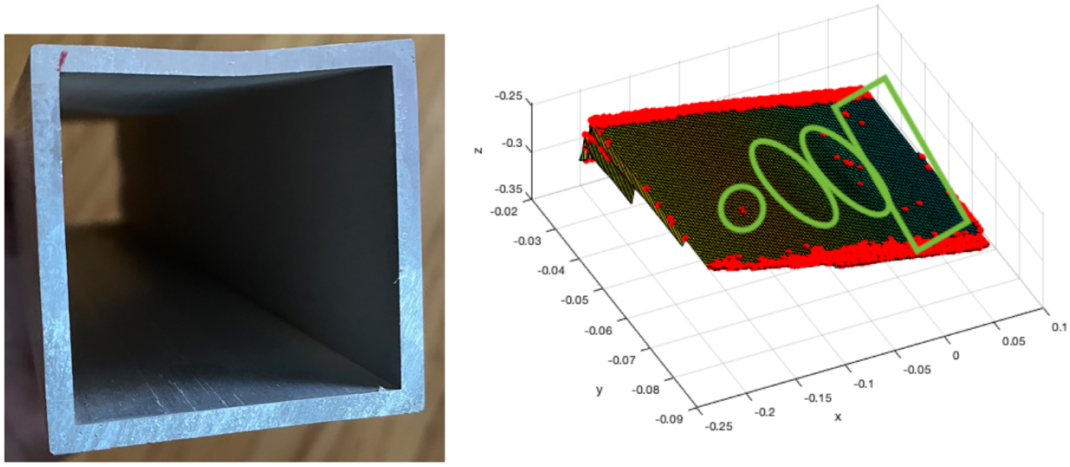

(a) One of the visible dents in the hammered object

(b) Results of the hammered object object

Figure 6.2: Hammered object with results

The results of the hammered object show grouping around the larger of two dents. The grouping is not very strong and may have been considered random if not for the visible dent in the gradient plot. It is difficult to see the smaller dent in Fig. 6.2a but it can be more easily viewed in Fig. 6.2b. The smaller dent was not detected as the threshold conditions were not met. This means that the slope of the dent was too shallow to be detected. Interestingly though, a small grouping can be seen in the lower left quadrant of Fig. 6.2b. This damage was created by hammering the tip of a screwdriver into the aluminum surface and can be seen as an RGB image in Fig. 6.3 below. Rather than having a shallow slope, the screwdriver dents create a more significant change in the surface.

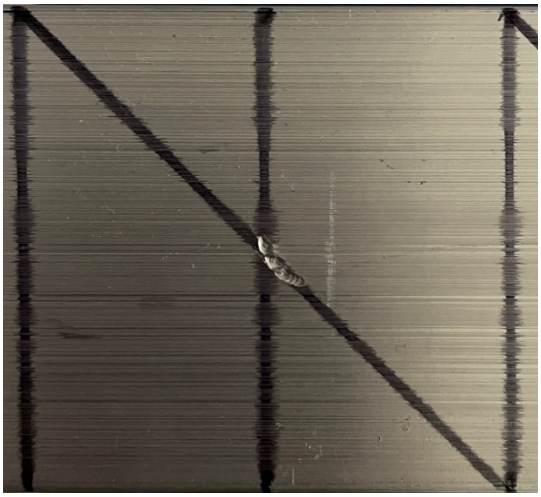

Figure 6.3: Damage created by screwdriver and hammer

6.1.2 Analysis of Drilled Objects

Figure 6.4 below shows the results of the drilled object. Again, damage detection around the edges of the object can be seen and are an expected result. By increasing the threshold slightly, the edge detection can be reduced. However, increasing the threshold may also result in damage no longer being detected as seen in Fig. 6.4a and Fig. 6.4b.

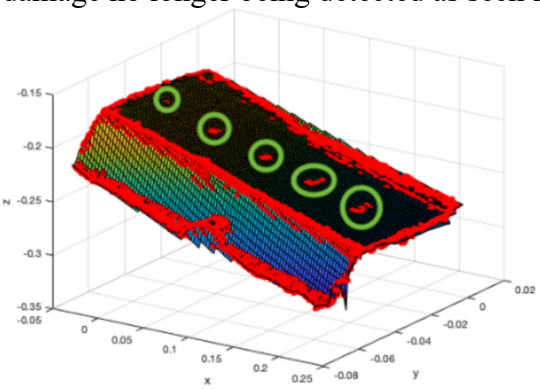

(a) Drilled object with threshold of 5

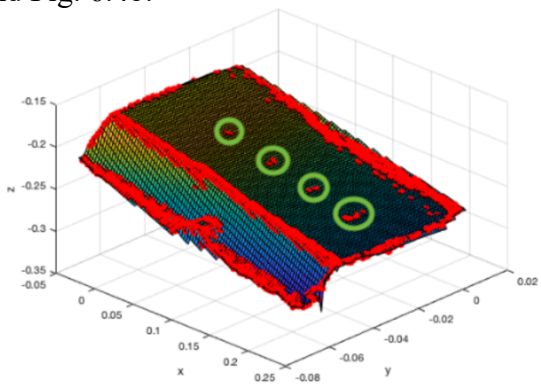

(b) Drilled object with threshold of 7

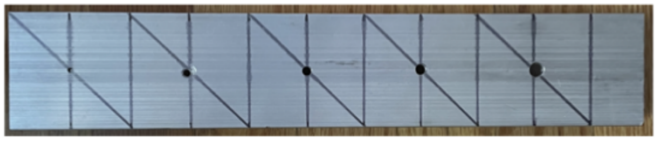

(c) Drilled object with five holes

Figure 6.4: Drilled object with results

Increasing the threshold by two degrees, reduced the number of points along the edge that were detected by the MATLAB script. However, Fig. 6.4a accurately shows the location of all five drill holes, while Fig. 6.4b only shows four drill holes. The smallest of the holes is 5/64 inch or 1.98 mm wide. To add some perspective, a grain of rice is about 2.05 mm wide [102]. Considering the image quality issues and the threshold constraints, it was surprising to see all five holes detected. This proves that this damage detection method is accurate on holes as small as 5/64 inch, or the thickness of a grain of rice.

6.2 Results of Aircraft Examples

Aircraft arrive and depart every day from the airport; however, the individual aircraft and the type of aircraft are not controllable variables. Only 737 and A320/A319 aircraft were accessible, and often the exact same aircraft is seen multiple times a week, or even multiple times a day. Additionally, aircraft with significant damage are often deemed unairworthy, and require maintenance repairs before they can be flown again. The airport that was accessible for this research is not a maintenance hub and therefore does not perform extensive repairs. For these reasons, the damage types available for research purposes was limited.

6.2.1 Undamaged Panel Analysis

To ensure that the results obtained from the MATLAB script were legitimate, an undamaged A319 fuselage panel was analyzed. From Fig. 4.3 it can be seen that the panel image

is of poor quality as the surface appears textured. After processing the image via MeshLab and running it through MATLAB, the results can be seen in Fig. 6.5 below.

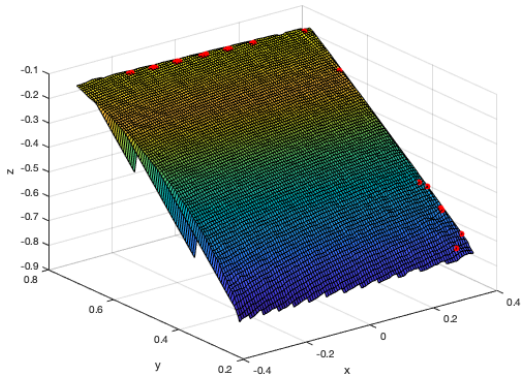

Figure 6.5: Results of undamaged panel

The pre-analysis processing helped clean up the edges, although there is still some edge detection seen at the top and right side of the panel. To achieve these results the threshold was set to 25 degrees. This threshold may seem high but when compared against the rest of the test surfaces, it is within a similar range. Overall, the expectation for the undamaged panel was to not have any damage detected, and after reviewing the results, this expectation was achieved.

6.2.2 Aircraft Dent Results

Figure 6.6 shows a 737 cargo bin door that was damaged. The damage is a shallow and small dent, about the size and thickness of a quarter. Cargo bin doors are a hot spot for damage as equipment and luggage make contact with the doors multiple times a day. The ability to detect damage along a cargo bin door is crucial to safely service and operate an aircraft on a daily basis.

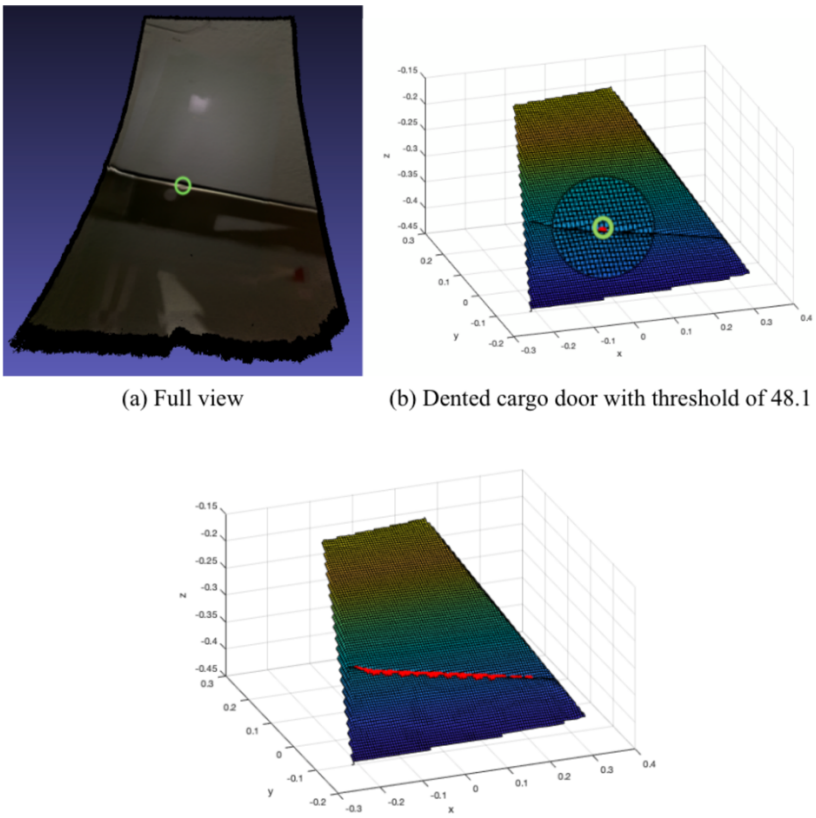

(a) Full view

(b) Dented cargo door with threshold of 48.1

(c) Dented cargo door with threshold of 25

Figure 6.6: 737 cargo bin door dent results

Figure 6.6 above shows the results of the dented cargo door. Unlike the more simply shaped aluminum square tubing, the edges of the cargo bin surface are not heavily detected. The natural curve of the cargo bin and the surrounding fuselage are not detected as there is no corner or edge to be detected. This clear and well-defined result is due in part to the image quality, as this image was one of the highest quality images captured.

When closed, cargo bin doors do not sit perfectly flush with the fuselage. Both the door itself and the surrounding fuselage edges are rounded. These rounded edges cause a small seam, or gap, to be visible along the surface. A smaller threshold of 25 allows for the detection of the entire cargo bin door seam. Whereas a larger threshold of 48.1 only detects the damaged area, ignoring the undamaged seam. Both results are useful.

Seams are normal and can be seen all over the exterior of the aircraft. The ability to detect an aircraft seam creates opportunity to also monitor the size of the seam. If a panel or door is beginning to loosen, being able to view and monitor the size of the gap can help prevent more significant damage from occurring. Additionally, being able to detect the damage entirely by itself, especially when the damage is so small, is further testament to the accuracy of this damage detection method.

6.2.3 Aircraft Component Analysis

Capturing an image of aircraft damage that resulted in a hole in the exterior skin of the aircraft was not feasible. As mentioned previously, access to an aircraft maintenance hangar was not available. Physically creating the damage was also not an option. The next best option for gathering images of a hole in an aircraft exterior was to collect images of a fluid port.

A potable water drain port was used in place of a hole caused by damage. The potable water drain is part of the aircraft; therefore, this is not an actual damaged surface. Regardless, the expected result was that the MATLAB script would detect the hole, and with a lower threshold, would also detect the dip that occurs along the surface. The results can be seen in Fig. 6.7 below.

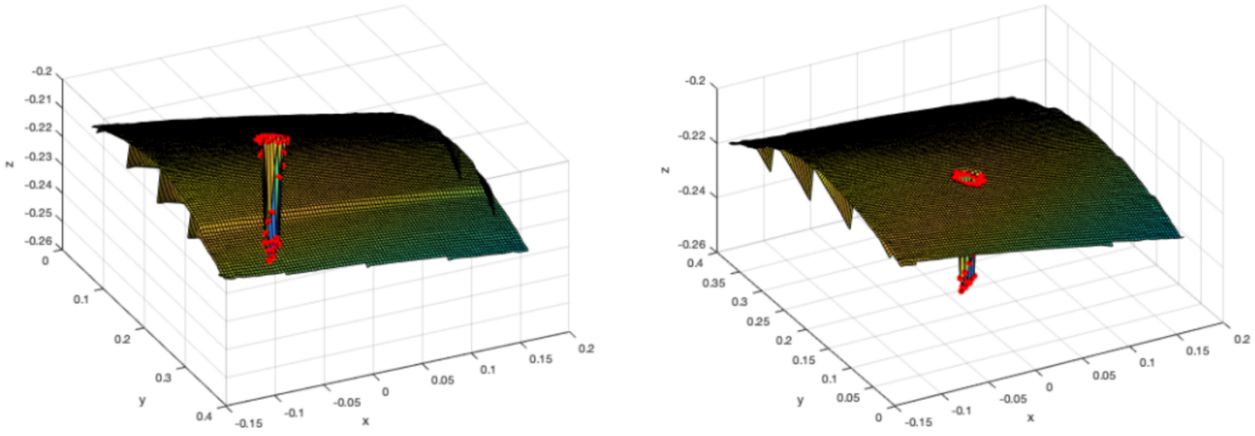

(a) Bottom view of aircraft hole results (b) Top view of aircraft hole results

Figure 6.7: Drain port results with threshold of 12

Images of the potable water drain port were fair quality. The edges are not as well defined as the cargo bin door images, however the detection around the edges is still minimal. Figure 5.3 is the same potable water drain analyzed with a threshold of 5 rather than 12. The results are as expected, with the hole and the dip in the surface both being detected. At the higher threshold, the edges are not detected at all, yet at the lower threshold some minor detection at the edges occurs.

7. Conclusion

Through the utilization of surface normals and the angles between vectors, the damage detection method outlined in this paper has performed better than expected. Large areas of damage were detected as expected but being able to detect holes as small as a grain of rice was a surprising result. For the square aluminum tubing, detection at the edges was caused by the large change in vector angles at the corners of the object. In real world applications the detection at the edges can create problems. Further research would be needed to determine how best to mitigate this false positive result. For the aircraft, the detection at the edges seemed to be caused by poor image quality and an incomplete surface image. Moving the camera perfectly to capture a clear and well-defined image was very difficult but also necessary to mitigate detection at the edge.

As mentioned in section I, the goal of this research was to use the advancements in inspection methodology and demonstrate their effectiveness in aircraft exterior inspections. In this regard, the project was a success. Apple's TrueDepth camera, a technology that is only four years old, was used to inspect the exterior of an aircraft and did so with a consistent effectiveness. As successful as this project was, there are still some limitations to consider.

7.1 Current Analytical Limitations

A useful feature of the MATLAB script would be to calculate the size of the damage from the area detected. However, no such feature currently exists, nor is it possible to determine the size manually. When the objects are imported into MeshLab, their dimensions are given as world units. MeshLab does not use any specific unit of measure; world units are simply used to proportionally display the object. Setting dimensions in MeshLab is feasible, however it still may not help with determining the size of the damage. As seen in Fig. 6.4a and Fig. 6.6a, very small areas of damage may result in a single red dot appearing. The size of the dot is set automatically by MATLAB and is not a usable factor in determining the size of the damage.

Consistent detection at the edges of objects is another limitation. Not only do edges consistently result in a false positive detection, but they may cause actual damage to be ignored. If there was damage along the edge of an object, it would likely be ignored due to the false positive results that occur, and are ignored, at the edges. Additional condition statements may be helpful to mitigate this. For instance, adding a condition statement to detect only vectors that face another vector along a specified boundary, may help with detection at an outer edge.

7.2 Potential Use Cases

The most obvious potential use case for damage detection would be to integrate it with a drone. A drone can range dramatically in size and design but one thing stands true for all drones, they are unmanned aerial vehicles (UAVs) and are controlled via remote control, fully autonomous systems, or a combination of the two [103]. Due to the wide range in commercially available drones, the range in payload capabilities is also large with a maximum of 1452 kg to a minimum of 0.2 kg [104]. The iPhone 12 Pro, used heavily for this research, has a weight of 189 grams or 0.19 kg, and is within the acceptable payload range regardless of the size of the drone [105]. Additional components may be required to fully integrate the non-destructive inspection

capabilities of the iPhone onto a drone and the additional payload requirements would need to be considered.

Increasing the payload would likely lead to tradeoffs. As the size of the drone increases, so will the required distance from the aircraft being inspected, thus increasing the visual requirements of the attached camera. The range and flight time of a drone also increases with size [104]. However, range and flight time may not be as important as camera quality when used in the aviation industry. If an inspection takes longer than a typical walkaround inspection, the usefulness of the damage detection integrated drone will decline.

Integration with drones would open even more potential uses for the damage detection analysis. Not only could the drones be used to inspect commercial aircraft, but as the Urban Air Mobility (UAM) industry grows, the need to inspect multiple vehicles quickly and effectively will grow with it. Additionally, the drones could be used in other industries for various structural inspections.

Lastly, integrating the damage detection script with a mobile phone may be a viable use case. Drones are useful, but they do require some initial setup and familiarity with the control system. Mobile phones are portable, easy to use, and there are several image processing applications available for download. Phones are already capable of capturing depth images and image processing, the only step missing is the image analysis. By integrating the final step with a mobile phone, the entire damage detection process can be completed in the palm of your hand.

References

[1] M. Edwards, "The History of the Pre-Flight Checklist," Aero Crew News, [Online]. Available: https://www.aerocrewnews.com/monthly-features/special-features/the-history-of-the-pre-flight-checklist/

[2] R. Bohn, "Not Flying By the Book: Slow Adoption of Checklists and Procedures in WW2 Aviation," 2013. [Online]. Available: https://art2science.files.wordpress.com/2013/07/standard-proced-adoption-bohn-2013.pdf

[3] K. Schabowicz, "Non-Destructive Testing of Materials in Civil Engineering," *Materials,* vol. 12, p. 3237, Oct. 2019.

[4] B. Kasal, M. Drdácký and I. Jirovsky, "Semi-destructive methods for evaluation of timber structures," *Advances in Architecture,* vol. 15, pp. 835-842, Jan. 2003.

[5] R. Ross and R. Pellerin, "Nondestructive Nondestructive Testing for Assessing Testing for Assessing Wood Members in Wood Members in Structures Structures A Review A Review," pp. 1-28, Jan. 1994.

[6] B. Rohner, H. Bugmann and C. Bigler, "Towards non-destructive estimation of tree age," *Forest Ecology and Management,* vol. 304, p. 286–295, Sept. 2013.

[7] A. U. Khan, "Non-Destructive Testing Applications in Commercial Aircraft Maintenance," *Forest Ecology and Management,* vol. 4, no. 6, June 1999.

[8] S. Dwivedi, M. Vishwakarma and A. Soni, "Advances and Researches on Non Destructive Testing: A Review," *Materials Today: Proceedings,* vol. 5, pp. 3690-3698, Jan. 2018.

[9] B. Raj, T. Jayakumar and P. C. Bhagi, "Non-destructive testing and evaluation for structural integrity," *Sadhana,* vol. 20, pp. 5-38, Feb. 1995.

[10] R. Gordon, "Acceptable Methods, Techniques, and Practices-Aircraft Inspection and Repair," Aug. 1998.

[11] V. Minutolo, S. Di Ronza, C. Eramo, P. Ferla, S. Palladino and R. Zona, "The Use of Destructive and Non-Destructive Testing in Concrete Strength Assessment for a School Building," *International Journal of Advanced Research in Engineering & Technology,* vol. 10, pp. 252-265, Dec. 2019.

[12] H. Sadek, "NDE technologies for the examination of heat exchangers and boiler tubes - Principles, advantages and limitations," *Insight,* vol. 48, pp. 181-184, March 2006.

[13] J. Krautkrämer and H. Krautkrämer, Ultrasonic Testing of Materials, 4 ed., Springer, 1990, pp. 192-198.

[14] H. Towsyfyan, A. Biguri, R. Boardman and T. Blumensath, "Successes and challenges in non-destructive testing of aircraft composite structures," *Chinese Journal of Aeronautics,* vol. 33, Sept. 2019.

[15] S. Verma, S. Bhadauria and S. Akhtar, "Review of Nondestructive Testing Methods for Condition Monitoring of Concrete Structures," *Journal of Construction Engineering,* vol. 2013, April 2013.

[16] J. Stump, "Nondestructive Inspection: The Big Five," Feb. 2003. [Online]. Available: https://www.aviationpros.com/home/article/10387212/nondestructive-inspection-the-big-five

[17] J. Blitz and G. Simpson, *Ultrasonic Methods of Non-destructive Testing,* Chapman and Hall, 1996.

[18] A. Uludag, "The Magnetic Particle Inspection Examination of Aircraft Propeller Mounting Bolts," *Journal of Multidisciplinary Engineering Science and Technology,* vol. 3, no. 12, Dec. 2016.

[19] "Magnetic Particle Testing," June 2021. [Online]. Available: https://www.pfinder.de/en/ndt-testing/magnetic-particle-testing/

[20] S. Worthington, "Magnaflux Testing," 2021. [Online]. Available: https://ecclestonaviation.co.uk/magnaflux-testing/?v=79cba1185463

[21] A. Hijazi, "Introduction to Non-Destructive Testing Techniques," [Online]. Available: https://sites.google.com/view/alahijazi/classes/non-destructive-testing-ndt

[22] M. Ben Gharsallah and E. Braiek, "Weld Inspection Based on Radiography Image Segmentation with Level Set Active Contour Guided Off-Center Saliency Map," *Advances in Materials Science and Engineering,* vol. 2015, pp. 1-10, Dec. 2015.

[23] W. Cheng, "Electromagnetic nondestructive evaluation of defects in ferromagnetic structures," *AIP Conference Proceedings,* vol. 1806, p. 110024, Feb. 2017.

[24] A. Birring, "Selection of NDT Techniques for Inspection of Heat Exchanger Tubing," *Materials Evaluation,* vol. 59, March 2001.

[25] A. Birring and G. Marshall, "Eddy Current Testing in the Petrochemical Industry," *Materials Evaluation,* vol. 61, pp. 1190-1195, Nov. 2003.

[26] S. Hewerdine, "Plant Integrity Assessment by the Acoustic Emission Testing Method," *Materials Evaluation,* 1993.

[27] A. Anastasopoulos, D. Kourousis and P. Cole, "Acoustic Emission Inspection of Spherical Metallic Pressure Vessels," April 2012.

[28] V. Leelalerkiet, T. Shimizu, Y. Tomoda and M. Ohtsu, "Estimation of Corrosion in Reinforced Concrete by Electrochemical Techniques and Acoustic Emission," *Journal of Advanced Concrete Technology,* vol. 3, pp. 137-147, Feb. 2005.

[29] "Diagnostic Acoustic Emission Solutions for Safety and Performance," 2016. [Online]. Available: http://www.idinspections.com/acoustic-emission-phenomenon/

[30] A. Kohan, Boiler Operator's Guide, 4 ed., McGraw-Hill Professional, 1997, p. 240.

[31] "Seal Aviation Dye Penetrant NDT Services," 2019. [Online]. Available: https://www.sealaviation.com/dye-penetrant

[32] P. Antunes, D. Duarte, B. Serrano, P. Pereira, G. Gameiro, M. Tavares, N. Ferreira, J. Viana, V. Infante and F. Moleiro, *Applicability of an Electromechanical Impedance NDT Equipment for Aeronautical Applications,* 2017.

[33] A. Pregelj, M. Drab and M. Mozetic, "Leak Detection Methods and Defining the Sizes of Leaks," *Slovenian Society for Nondestructive Testing,* vol. 4, no. 2, Feb. 1999.

[34] R. Gordon, "Visual Inspection for Aircraft," Aug. 1997.

[35] American Airlines, "737 Max Return to Service," [Online]. Available: https://www.aa.com/i18n/travel-info/737-MAX-return-to-service.jsp

[36] J. Asquith, "Analysis - How Much Money Do Empty Flights Really Cost Airlines," Forbes, March 2020. [Online]. Available: https://www.forbes.com/sites/jamesasquith/2020/03/31/

analysis-how-much-money-do-empty-flights-really-cost-airlines/?sh=3d5f8c2b5854

[37] P. Vitoriano and T. Amaral, "3D Solder Joint Reconstruction on SMD based on 2D Images, " *SMT Surface Mount Technology Magazine,* vol. 31, July 2016.

[38] L. Wasserman, "Rise of the Machines," *Past, Present and Future of Statistical Science,* pp. 525-536, 2014.

[39] H. Mac, H. Tran, J. Huh, N. Doan, C. Kang and D. Han, "Detection of Delamination with Various Width-to-depth Ratios in Concrete Bridge Deck Using Passive IRT: Limits and Applicability," *Materials,* vol. 12, p. 3996, Dec. 2019.

[40] R. Adhikari, O. Moselhi and A. Bagchi, "Image-Based Retrieval of Concrete Crack Properties," June 2012.

[41] S. Kawabata, K. Nohara, J. Lee, H. Suzuki, T. Takiguchi, O. S. Park and S. Okamoto, "Autonomous Flight Drone with Depth Camera for Inspection Task of Infra Structure," vol. 2, 2018.

[42] T. Mitsa, "How Do You Know You Have Enough Training Data?," *Towards Data Science,* April 2019.

[43] E. Mishra, N. Anwar, M. Amir Izhar and S. Supprasert, "Image Based Inspection and Monitoring of Buildings," Sept. 2019.

[44] B. Spencer, V. Hoskere and Y. Narazaki, "Advances in Computer Vision-Based Civil Infrastructure Inspection and Monitoring," *Engineering,* vol. 5, pp. 199-222, March 2019.

[45] Intel, "Beginner's Guide to Depth (Updated)," [Online]. Available: https://www.intelrealsense.com/beginners-guide-to-depth/#:~:text=Structured\%20light\%20and\%20coded\%20light\%20depth\%20cameras\%20are\%20not\%20identical,some\%20combination\%20of\%20the\%20two

[46] Eyerys, "How Apple's LiDAR Sensor Differs From The One On Its 'TrueDepth' Face ID," [Online]. Available: https://www.eyerys.com/articles/how-apples-lidar-sensor-differs-one-its-truedepth-face-id

[47] A. McWilliams, "How a Depth Sensor Works - in 5 Minutes," Aug. 2013. [Online]. Available: https://jahya.net/blog/how-depth-sensor-works-in-5-minutes/#:~:text=The\%20IR\%20projector\%20projects\%20a,of\%20dots\%20in\%20infra\%2Dred

[48] Intel, "Depth Camera D435," [Online]. Available: https://www.intelrealsense.com/depth-camera-d435/

[49] D. Mader, R. Blaskow, P. Westfeld and C. Weller, "Potential of UAV-Based Laser Scanner and Multispectral Camera Data in Building Inspection," *ISPRS - International Archives of the Photogrammetry, Remote Sensing and Spatial Information Sciences,* Vols. XLI-B1, pp. 1135-1142, June 2016.

[50] J. K. Chow, Z. Su, J. Wu, Z. li, P. S. Tan, K.-f. Liu, X. Mao and Y.-H. Wang, "Artificial intelligence-empowered pipeline for image-based inspection of concrete structures," *Automation in Construction,* vol. 120, p. 103372, Dec. 2020.

[51] A. Khaloo, D. Lattanzi, K. Cunningham, R. Dell'Andrea and M. Riley, "Unmanned aerial vehicle inspection of the Placer River Trail Bridge through image-based 3D modelling," *Structure and Infrastructure Engineering,* vol. 14, pp. 1-13, May 2017.

[52] R. Almadhoun, T. Taha, L. Seneviratne, J. Dias and G. Cai, "A survey on inspecting structures using robotic systems," *International Journal of Advanced Robotic Systems,*

vol. 13, 2016.

[53] K. Malandrakis, A. Savvaris, J. Gonzalez-Domingo, N. Avdelidis, P. Tsilivis, F. Plumacker, L. Zanotti Fragonara and A. Tsourdos, "Inspection of Aircraft Wing Panels Using Unmanned Aerial Vehicles," Aug. 2018.

[54] J. Beyerer, F. León and C. Frese, *Machine vision: Automated visual inspection: Theory, practice and applications,* 2015, pp. 1-798.

[55] J. F. Ebersole, "Optical Image Subtraction," *Optical Engineering,* vol. 14, no. 5, pp. 436-447, 1975.

[56] J.-c. Jeong, H. Shin, J. Chang, E.-G. Lim, S. M. Choi, K.-J. Yoon and J.-i. Cho, "High-Quality Stereo Depth Map Generation Using Infrared Pattern Projection," *ETRI Journal,* vol. 35, no. 6, pp. 1011-1020, 2013.

[57] A. Grunnet-Jepsen, J. N. Sweetser, P. Winer, A. Takagi and J. Woodfill, "Projectors for D400 Series Depth Cameras," 2020. [Online]. Available: https://www.intelrealsense.com /wp-content/uploads/2019/03/WhitePaper_on_Projectors_for_RealSense_D4xx_1.0.pdf?_ ga=2.190575083.1331233386.1626213982-452489180.1625897375

[58] D. Asamoah, E. Oppong, S. Oppong and J. Danso, "Measuring the Performance of Image Contrast Enhancement Technique," *International Journal of Computer Applications,* vol. 181, pp. 6-13, Oct. 2018.

[59] L. Lin, Z. Demirbilek, H. Mase and F. Yamada, "CMS-Wave: A Nearshore Spectral Wave Processes Model for Coastal Inlets and Navigation Projects," p. 132, Aug. 2008.

[60] Boeing, "The 747 Family Plan," May 2010. [Online]. Available: https://www.boeing.com/ resources/boeingdotcom/company/about_bca/startup/pdf/historical/747-400-passenger.pdf

[61] S.-M. An, R. Ramesh, Y.-S. Lee and W.-Y. Chung, "Interaxial Distance and Convergence Control for Efficient Stereoscopic Shooting using Horizontal Moving 3D Camera Rig," *International Journal of Electrical and Computer Engineering,* vol. 5, no. 11, pp. 1399 - 1404, 2011.

[62] A. Lipnickas and A. Knyš, "A Stereovision System for 3-D Perception," *Elektronika ir Elektrotechnika,* pp. 1215-1392, April 2009.

[63] R. Orozco, C. Loscos, I. Martín and A. Artusi, "Multiview HDR Video Sequence Generation," p. 630, April 2016.

[64] D. Scharstein, R. Szeliski and R. Zabih, "A taxonomy and evaluation of dense two-frame stereo correspondence algorithms," pp. 131-140, 2001.

[65] P. Serafinavičius, S. Sajauskas and G. Daunys, "Evaluation of Hand Pointing System Based on 3-D Computer Vision," *Elektronika ir Elektrotechnika,* pp. 1215-1392, Jan. 2008.

[66] O. Faugeras, "Three-dimensional computer vision: a geometric viewpoint," *MIT press,* Jan. 1993.

[67] P. Munro and A. Gerdelan, "Stereo Vision Computer Depth Perception," 2006.

[68] J. Starr and B. Lattimer, "A comparison of IR stereo vision and LIDAR for use in fire environments," *Proceedings of IEEE Sensors,* pp. 1-4, Oct. 2012.

[69] J. Cipriani, "iPhone Face ID is Pretty Cool. Here's How it Works and How to Use it," Feb. 2020. [Online]. Available: https://www.cnet.com/tech/services-and-software/the-iphone-and-ipads-face-id-tech-is-pretty-darn-cool-heres-how-it-works-and-how-to-use-it/

[70] M. Vogt, A. Rips and C. Emmelmann, "Comparison of iPad Pro®'s LiDAR and TrueDepth Capabilities with an Industrial 3D Scanning Solution," *Technologies,* vol. 9, no. 2, p. 25, 2021.

[71] Apple Insider, "Face ID," March 2021. [Online]. Available: https://appleinsider.com/inside/face-id

[72] D. Houcque, "Introduction to Matlab for Engineering Students," Northwestern University, 2005.

[73] "Stem3," [Online]. Available: https://www.mathworks.com/help/matlab/ref/stem3.html?searchHighlight=stem3&s_tid=srchtitle

[74] "Quiver3," [Online]. Available: https://www.mathworks.com/help/matlab/ref/quiver3.html

[75] "Surf," [Online]. Available: https://www.mathworks.com/help/matlab/ref/surf.html?s_tid=doc_ta

[76] "Surfnorm," [Online]. Available: https://www.mathworks.com/help/matlab/ref/surfnorm.html?searchHighlight=surfnorm&s_tid=srchtitle

[77] "isInsideSubMap," [Online]. Available: https://www.mathworks.com/help/vision/ref/pcmapndt.isinsidesubmap.html?searchHighlight=isinside&s_tid=srchtitle

[78] "isChange," [Online]. Available: https://www.mathworks.com/help/matlab/ref/ischange.html?searchHighlight=ischange&s_tid=srchtitle#mw_726ba8c8-e01f-444d-98bb-0b008e7f3885

[79] R. Fisher, P. S., A. Walker and E. Wolfart, "Pixel Subtraction," *Image Processing Learning Resources,* 2003.

[80] D. Girardeau-Montaut, "How to Compare Two 3D Entities," Feb. 2015. [Online]. Available: https://www.cloudcompare.org/doc/wiki/index.php?title=How_to_compare_two_3D_entities

[81] A. Grunnet-Jepsen, J. Sweetser, T. Khuong, S. Dorodnicov, D. Tong and O. Mulla, "Intel® RealSense™ Self-Calibration for D400 Series Depth Cameras," 2019. [Online]. Available: https://dev.intelrealsense.com/docs/self-calibration-for-depth-cameras

[82] "Graphics Language (GL) Transmission Format (glTF) Family," Sustainability of Digital Formats: Planning for Library of Congress Collections, June 2019. [Online]. Available: https://www.loc.gov/preservation/digital/formats/fdd/fdd000498.shtml

[83] A. Simkin, "glTF – Behind the scene of 3D Magic," Nov. 2019. [Online]. Available: https://stayrelevant.globant.com/en/gltf-behind-the-scene-of-3d-magic/

[84] "STL (STereoLithography) File Format Family. Also referred to as "Standard Triangle Language" and "Standard Tessellation Language."," Sustainability of Digital Formats: Planning for Library of Congress Collections, Sept. 2020. [Online]. Available: https://www.loc.gov/preservation/digital/formats/fdd/fdd000504.shtml

[85] T. Grim, User's Guide to Rapid Prototyping, Dearborn, MI: Society of Manufacturing Engineers, 2004, p. 55.

[86] C. K. Chua, K. F. Leong and C. S. Lim, Rapid Prototyping: Principles and Applications, World Scientific Publishing Co, 2003, p. 237.

[87] M. Burns, "Automated fabrication: The future of manufacturing," *International Congress on Applications of Lasers \& Electro-Optics,* vol. 1994, no. 1, pp. 1-5, 1994.

[88] G. Turk, "The PLY Polygon File Format," 1994. [Online]. Available: https://www.loc.gov/preservation/digital/formats/fdd/fdd000501.shtml

[89] R. Wanhill and G. Bray, "Chapter 2 - Aerostructural Design and Its Application to Aluminum–Lithium Alloys," in *Aluminum-lithium Alloys*, N. E. Prasad, A. A. Gokhale and R. Wanhill, Eds., Boston, Butterworth-Heinemann, 2014, pp. 27-58.

[90] "Material Properties Data: 6061-T6 Aluminum," May 2020. [Online]. Available: https://www.makeitfrom.com/material-properties/6061-T6-Aluminum

[91] "Aircraft and Aerospace Applications: Part One," March 2004. [Online]. Available: http://www.totalmateria.com/Article95.htm

[92] "Standard Specification for Aluminum and Aluminum-Alloy Sheet and Plate (Metric)," Aug. 2014.

[93] "3 Metallic Materials and Processes," pp. 26-35, 1996.

[94] "Aluminum Alloys," [Online]. Available: https://www.experimentalaircraft.info/articles/aircraft-aluminum.php

[95] "Aluminum Alloys 101," [Online]. Available: https://www.aluminum.org/sites/default/files/2021-09/AA-Infographic-Alloys-v5_0.jpg

[96] "7050 Aluminium Technical Datasheet," 2018. [Online]. Available: https://www.smithmetal.com/pdf/aluminium/7xxx/7050.pdf

[97] "Aluminium / Aluminum 7050 Alloy (UNS A97050)," Sept. 2012. [Online]. Available: https://www.azom.com/article.aspx?ArticleID=6650

[98] "Aluminum 7050," [Online]. Available: https://continentalsteel.com/aluminum/grades/alloy-7050/

[99] "ASM Handbook Volume 2: Properties and Selection: Nonferrous Alloys and Special-Purpose Materials," Oct. 1990.

[100] "Aluminum 7075-T6; 7075-T651," May 2004. [Online]. Available: https://web.archive.org/web/20191019031041/http://asm.matweb.com:80/search/SpecificMaterial.asp?bassnum=MA7075T6

[101] Maintenace & Engineering Center, "Ramp Operations Manual," *AA Web Reference,* 2021.

[102] S. Reidy, "Rice Thickness Grading," 2015. [Online]. Available: https://www.world-grain.com/articles/5741-rice-thickness-grading

[103] L. Cary and J. Coyne, "Unmanned Aircraft Systems (UAS)," *Circular 328,* 2011.

[104] "The Drone Database," [Online]. Available: http://drones.cnas.org/drones/

[105] "Comparing iPhone 12 models: Every difference between Apple's iPhone 12, Mini, Pro and Pro Max," Sept. 2021. [Online]. Available: https://www.cnet.com/tech/mobile/iphone-12-differences-apple-iphone-12-mini-pro-max/

Appendix A – MatLab Script for Damage Detection

```
%% Dataset

V = YourFileHere;

%% Shaping the data

% Separating the columns to be axis specific
x1 = V(:,1);
y1 = V(:,2);
z1 = V(:,3);

% Defining the step size and converting to a mesh from general coordinates
xv = linspace(min(x1), max(x1), 100);
yv = linspace(min(y1), max(y1), 100);
[X,Y] = meshgrid(xv, yv);
Z = griddata(x1,y1,z1,X,Y);

% Note: 100 is the stepsize and will determine the size of the matrices

%% Calculations

% Surfnorm calculates the surface normals of the vertices
[Nx,Ny,Nz] = surfnorm(X,Y,Z);
% Quiver3 displays the normals
figure()
quiver3(X,Y,Z,Nx,Ny,Nz);

% Creating empty matrix to be filled with angle values in degrees
angledata=zeros(100);
% Creating empty matrix to be filled with logical values
zeroOne=zeros(100);

% Note: Matrix sizes are determined by the stepsize - 100

% Calculating the angle between surface normal
for i = 1:numel(Nx)-1
   pos = i; % position

   % Can only calculate angle between two vectors so looping thru each
   % position to calculate all the angles
   v1 = [Nx(pos);Ny(pos);Nz(pos)];
   v2 = [Nx(pos+1);Ny(pos+1);Nz(pos+1)];

   % Calculating cos(theta) from v1 and v2
```

```
    CosTheta= max(min(dot(v1,v2)/(norm(v1)*norm(v2)),1),-1);

    % Storing the angle data in degrees
    [angledata(pos)] = real(acosd(CosTheta));


    % Creating a threshold - if angle is larger than value, set zeroOne
    % value to 1
    if angledata(pos) > 5
        [zeroOne(pos)] = 1;

    end

end
```